A comprehensive analysis of buildability of 3D-printed concrete and the use of bi-linear stress-strain criterion-based failure curves towards their prediction

Avinaya Tripathi*, Sooraj A.O. Nair*, Narayanan Neithalath*

Abstract

The buildability of cementitious materials, along with its extrudability, determines the printability of the concrete mixtures used in 3D printing of concrete. Buildability, defined as the critical height to failure during printing, is a function of the material properties (time-dependent), filament dimensions, and print geometry. This study employs a novel approach to evaluate the buildability of 3D printed concrete using a combination of: (i) modified green compression test (GCT) carried out on cylinders extracted from 3D printed prisms (in lieu of cast cylinders) at different times from mixing to extract a bi-linear stress-strain response until the yield point, from which material properties are deduced, and (ii) models considering material failure (e.g., plastic collapse) or instability (e.g., buckling/crippling) that employ refined material parameters (elastic and initial plastic yield stresses and moduli) from GCT. Failure curves are developed for different 3D printable mortar mixtures using the lower bounds of failure heights at different times predicted by the different failure models. Laboratory-scale printing of wall and hollow cylinder elements showed that the models can adequately predict failure heights. The ability to accurately predict critical (failure) height enables enhanced control in optimizing the material design and printing process.

Keywords: 3D concrete printing; Buildability; Bi-linear response; Green Compression Test; Failure modes

^{*} Graduate student, School of Sustainable Engineering and Built Environment, Arizona State University, Tempe AZ 85287

[†] Professor, School of Sustainable Engineering and Built Environment, Arizona State University, Tempe AZ 85287; Corresponding author: e-mail: Narayanan.Neithalath@asu.edu

1. Introduction

3D-concrete printing is emerging as a promising construction technique for building even complex structural/architectural elements quickly and efficiently without formwork. The reduction in construction cost and wastage, and architectural and sustainability benefits of 3D printed concrete structures have been well-documented [1–3]. However, there are many challenges in using such an automated process in large-scale construction projects involving concrete. Among the major scientific challenges in 3D concrete printing, the notable ones relate to the material as such, especially its properties and their development in the fresh state, which interferes with the construction process in a major way. 3D concrete printing relies on extrusion of the fresh material through a nozzle, followed by stacking of the extrudate in layers to build up the structure [4]. This necessitates that the extrudate demonstrates time-dependent rheological and mechanical properties that comply with the extrudability and buildability requirements [5]. Extrudability is defined as the ability of a material to pass through an opening under pressure and retain its shape after extrusion [5], while buildability refers to the ability to develop adequate strength at any given section of a print to overcome the overburden pressure exerted by the subsequent layers without excessive deformation or failure [6,7]. The combination of extrudability and buildability can be termed as printability. It has been shown that a moderate yield stress is desirable for better extrudability [8], while a higher yield stress is favorable for better buildability [9]. It needs to be noted that 'moderate' and 'higher' are relative terms that depend on the process conditions (e.g., printer type - ram or screw extruder, print speed, vertical build-up rate etc.) as well. Appropriate binding materials, water content, and the use of chemical admixtures to ensure high particle packing helps in optimization of the material, whereas appropriate mixing processes, rest time, and printer characteristics forms part of the process optimization to ensure desired printability, on which the properties of the 3D printed concrete structure rely significantly on. Thus, it is evident that, understanding the material characteristics and the ability to predict its buildable height (buildability) is critical in mixture and process selection, as well as in developing specifications and quality control standards for fresh concrete to be used in 3D printing [10].

Since buildability is defined as the height to which a given material can be printed without failure for a certain cross-section geometry, it can be evaluated in a straightforward manner through trial prints of the chosen, extrudable material [7,11–14]. However, time-dependent material behavior when printed also needs to be related to the imposed loads (stresses) and material property development that enables buildability. To ensure accurate predictions, the material properties and their development, and the geometry of the printed element also needs to be considered. This has been attempted in the form of

prediction models for buildability. Failure of the printed structure in several previous studies is assumed to be caused mainly by the self-weight of the printed structure [15–17]. Material properties can be obtained from rheological tests [16–18] or uniaxial and/or triaxial compression tests [19–21] on the fresh material, the results of which can then be empirically correlated to buildability. Therefore, rheology-based models [17,22,23], mechanical property-based models [15,19–21], or a combination [24] have been employed for buildability prediction, with mixed results. In many of the cases, the tests are done for mixtures printed immediately after mixing. The elastic modulus of fresh concrete has been determined in accordance with a procedure based on ASTM D 2166 [19,25]. However, inaccuracies in determinations of material properties at early ages either through inadequate specimen preparation and testing methods, less robust testing procedures, or inaccurate data processing are likely to result in significant errors that seriously limit buildability predictions.

This paper focuses on developing an appropriate method to analyze and predict the buildability of 3D printable cementitious mixtures as a function of time from mixing, based on fresh-state uniaxial compression testing. The work is motivated by the observation that very careful sample preparation and controlled testing of fresh mixtures in a displacement-controlled mode at slow enough strain rates allow for the capture of a bi-linear stress-strain response, rather than the commonly used single slope to determine a single modulus for the fresh mixture. The initial linear response generally ends at less than 0.25% strain, which might be the cause for it being missed in many reported works. Using the parameters extracted from the bi-linear stress-strain response of the fresh mixtures at different ages, along with analytical models for different modes of failure of geometric elements due to overburden pressure, failure surfaces are created. These are then validated using experiments on printed wall and hollow columns. It is anticipated that the approach described in this paper can be reliably used in the analysis and assessment of buildability of different mixtures used for concrete 3D printing, paving the way for a test method for material qualification. This approach is based on the mechanics of build-up of soft solids, and also has the potential to be implemented as a test standard.

2. An Analytical Model for Buildability Assessment

Figure 1 shows a flow diagram to demonstrate how a bi-linear stress-strain model and the parameters extracted from it can be used to assess and predict the buildability of 3D printed concrete structural elements. The model is defined in three stages, which are elucidated in detail in this section. In the first stage, the material characteristics are identified using a bi-linear stress-strain response. In the second stage, stress states in individual layers as the structure is built-up is considered, while in the third stage

failure modes based on the considered model under which a printed structure fails, are evaluated. The material characteristics required for the model are the elastic modulus (E_e), plastic modulus (E_p), elastic yield stress (σ_e) and plastic yield stress (σ_p). Based on the material characteristics and geometrical properties of printed elements, the anticipated failure heights based on different failure modes are predicted. The stress growth during printing contributes to the assessment of whether a certain section in the print is under elastic or plastic response. Each of the stages in model development are discussed in detail in the forthcoming sections.

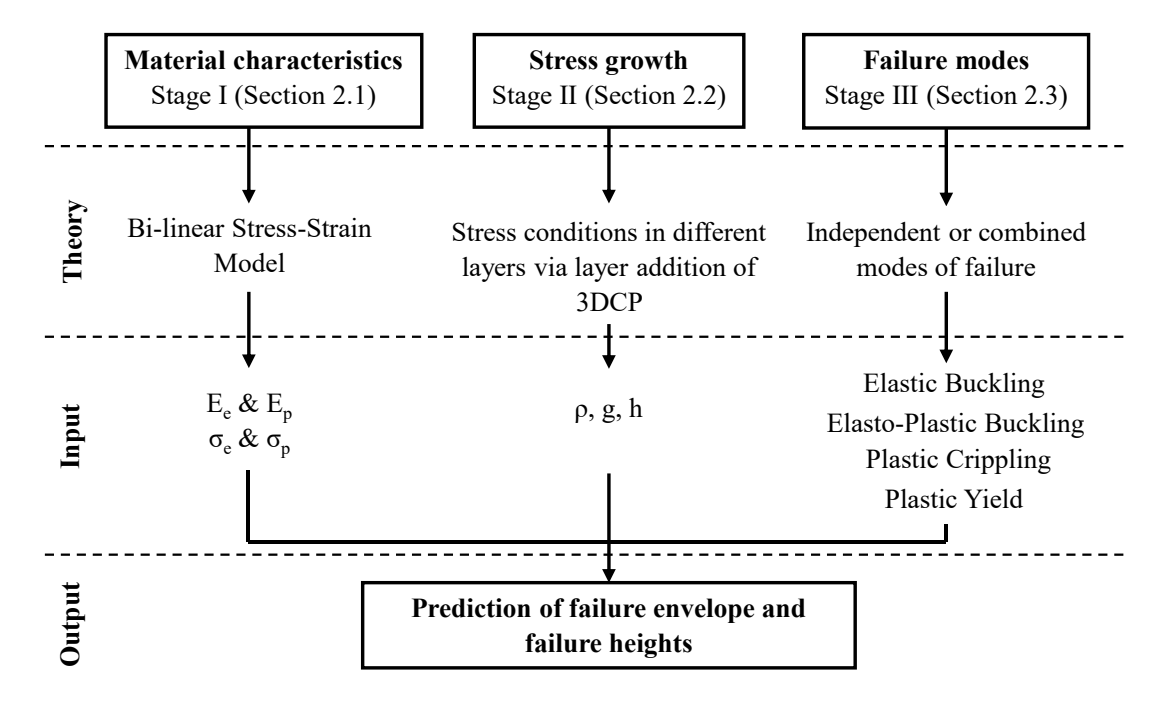


Figure 1: Flow diagram showing the stages in the buildability assessment model using a bi-linear stress-strain criterion and stress growth in layers during printing.

2.1 Material characteristics

The proposed failure prediction model uses material characteristics derived from the uniaxial compressive stress-strain response of a fresh 3D printable mortar. Green compression test (GCT) [24,25] is carried out on mortars in the fresh condition. Several variants of such a test have been reported in the literature, using different specimen sizes, and loading rates. It has been shown that GCT performed on compacted cylindrical mortar samples (70 mm diameter and 140 mm high) to obtain compressive strength and elastic modulus of 3D printed elements overestimates the material properties [25]. Efforts to test a printed filament 10 mm \times 30 mm \times 100 mm [24] have also not yielded accurate failure stresses because of

insufficient sample thickness. In general, the GCTs reported in the literature capture only the plastic response (which sometimes is termed as elastic response in many publications because it is the only modulus obtained) of the material, and the very early elastic response is undetected, plausibly due to higher strain rates used in testing (about 5% and 21% strain/min respectively in [24,25]), and inadequate surface contacts during testing.

A typical compressive stress-strain response of a fresh mortar, carried out under a slow loading rate (~ 1%/min), is illustrated in Figure 2, with specific points and regions of interest labeled. Note that only the general trend is shown here; individual experimental results could vary slightly depending on the mixture characteristics and testing conditions, as is shown later. As observed, the overall pre-peak response can be divided into an elastic and an initial plastic regime (even though the term 'secondary elastic regime' can be used, it is not used here to avoid confusion). If the test is carried out at a higher strain rate, the elastic modulus will be a composite of both the elastic and initial plastic slopes (closer to the elastic value if the initial tangent modulus is used, or closer to the plastic value if the secant modulus is used), as has been noticed in tests on fresh concrete. Elastic yielding of the material, as defined here, is not assumed to cause failure of the structure; rather it signifies the attainment of sufficient stress to induce flow and undergo a strain-hardening plastic deformation. During extrusion of a filament, the material is in a plastic flow state, which helps the material flow out of the nozzle, and retain its shape (based on the design filament dimensions and flow rate) as the plastic flow ceases. This filament can withstand small loads by undergoing small amounts of deflection, which corresponds to the elastic response of the material that lies within a very small strain range similar to the elastic range in other soft materials (e.g., gels, pastes, elastomers) [26,27], and is represented by the region until the elastic yielding stage shown in Figure 2. For such soft solids, under low strain rates, a bi-linear stress-strain response has been considered in previous works [28-31], even though the reasons for such considerations are different. For example, for biopolymers, the normal stress variation is a function of the network stress and fluid pressure [31], while for some other porous solids, the void morphology dictates the bi-linear response [28]. For layer-wise printing of a soft material, where multiple soft layers are subjected to incremental and differential loading during printing, the homogenous response achieved during GCT can be related to the process of layers being differentially loaded in actual printing, which justifies the use of a bi-linear response, as elucidated in this and the following sections. The elastic yield stress described here thus relates to the axial loading of the material already printed, through the superimposition of more material when deposited as layers (as opposed to shear and extrusional yield stresses that relate to the process of extruding uniform filaments out of the nozzle [7,17]). When loads due to printing of more layers is simulated by the

increasing load on the GCT specimen, stress in one or more of the bottom layers exceeds the elastic yield stress, and the material undergoes further deformation under load. This is denoted as the initial plastic response of the material. The purpose of defining a bi-linear stress-strain response considering elastic and initial plastic responses for an apparently plastic material is to ensure that the change in rate of deformation (strain) of a considered layer under increasing loads is adequately accounted for.

The slope of the linear portion of the stress-strain curve at very low strains is termed as the initial elastic modulus (E_e) , while the slope after the early inflection point (after which it is called the plastic regime, for ease of referencing) quantifies an apparent plastic modulus (E_p) , as shown in Figure 2. Elastic yield stress (σ_e) is identified as the point where the first significant change in slope occurs, while initial plastic yield stress (σ_p) is the critical stress beyond which the material starts experiencing further non-linearity. The elastic and initial plastic modulus (hereinafter referred to as plastic modulus) are estimated as the slopes of the linear portions in elastic and initial plastic regimes, respectively. Elastic yield stress is the maximum stress in the linear elastic regime whereas plastic yield stress demarcates the non-linear strain softening. Since the early elastic regime is bound by very narrow limits of stress and strain values (typically within 0.25% strain in this study), the test specimen preparation and the test procedure should be robust enough to capture this response during a GCT, which will be explained in a later section. The time-dependent strength and stiffness evolution that influences the print failure can be established by characterizing this stress-strain response at regular intervals after mixing [24,25]. This can then be used to calculate the failure heights in different failure modes (proposed in Section 2.3) and subsequently, the critical failure height at any given time is predicted as the absolute minimum height among these values.

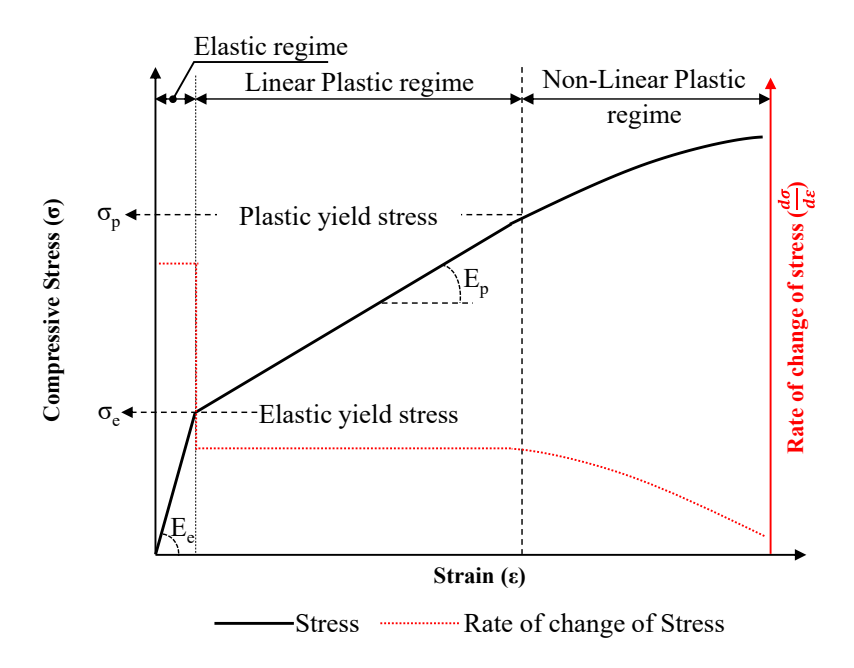


Figure 2: Typical bi-linear stress-strain response of fresh mortars under compression showing elastic and plastic regimes. Also shown are the quantifiable parameters used in the failure model including the elastic yield stress (σ_e), initial plastic yield stress (σ_p), elastic modulus (E_e), and initial plastic modulus (E_p)

2.2 Stress growth rate

The printing rate denotes the rate of vertical build-up of a structure during printing, and depends on the print geometry, filament dimensions, and print nozzle speed. The printing rate thus governs the rate of stress growth in each layer as the printing progresses. The bottommost layer is subjected to the maximum overburden stress. However, since the failure model is based on a bi-linear stress-strain relationship, stress growth in each layer, that determines if a given layer is in elastic or initial plastic regime (as defined in Figure 2), is of importance. Figure 3 shows the conceptual representation of stress growth in different layers during a layered 3D printing process. In this staircase model of stress growth as a function of number of layers printed (or time), the tread indicates the duration of printing a certain layer (i.e., time elapsed between layer n and n+1), and the rise denotes the incremental stress on layer n due to the deposition of the layer n+1. As an example, the leftmost staircase in this figure represents the stress on the first (bottommost) layer. The vertical rises in this staircase corresponding to (2, 3...11) on the X-axis denotes the incremental stress on layer 1 when subsequent layers are placed. This constant stress increment can be calculated by dividing the weight of the individual filament by its plan area, and is given

$$Stress\ per\ layer\ =\ \frac{Filament\ Weight}{Filament\ Area}\ =\ \frac{\rho Vg}{A}\ =\ \frac{\rho(A\times\ h)g}{A}\ =\ \rho\times\ h\times\ g$$
 Eq. 1

where ρ is the density of material, A is the plan area of the layer, h is individual layer height, and g is the acceleration due to gravity. Note that the layer height, nozzle speed, and the plan area are assumed to remain constant for this calculation. In other words, the layer deformations due to overburden pressure are ignored in this idealized calculation scheme.



Figure 3: Schematic showing the stress growth in different layers with subsequent layer deposition. σ_e corresponds to the elastic yield limit obtained from the stress-strain response.

Considering the bottommost layer (layer 1), it can be noticed from the conceptual illustration in Figure 3 that, when the sixth layer is being laid, the stress in layer 1 exceeds the elastic yield stress (defined in Figure 2) and enters the initial plastic regime. As another layer is laid, the second filament from the bottom (layer 2) enters the initial plastic response regime. This process continues for each subsequent layer until complete print failure occurs. For example, when the ninth layer is being printed, layers 5-8 experience stresses below the elastic yield stress, while layers 1 to 4 experience stresses larger than σ_e . Thus, if failure does not occur before the stress in the bottommost layer approaches σ_e , it can be seen that a few layers on the top will be in the elastic regime, while few layers in the bottom would have already reached the initial plastic regime, as demonstrated in Figure 3. This indicates that, in this ideal case, a certain number of layers (from the topmost layer) are always subjected to stresses lower than the elastic yield stress, while the plastic response begins from the bottommost layer and propagates upwards as new layers are

added. Figure 4 depicts this idea, where dark-colored regions correspond to the layers where the vertical stress is lower than the elastic yield stress, and the light-colored regions correspond to the layers where the vertical stresses exceed the elastic yield stress. In the example mentioned above, there will be five layers (in the top) demonstrating elastic response, and all the layers below demonstrate plastic response when the 11th layer is printed. In this exercise, the time-dependent evolution of material properties has not been considered since the printing process (until the print fails) is completed within 10 min. The failure height (or number of layers until failure) is thus assigned to the print start time. In other words, a buildability of 100 mm at 0.5 h denotes that the printing process was started when the mixture was 0.5 h old (i.e., 0.5 h after mixing).

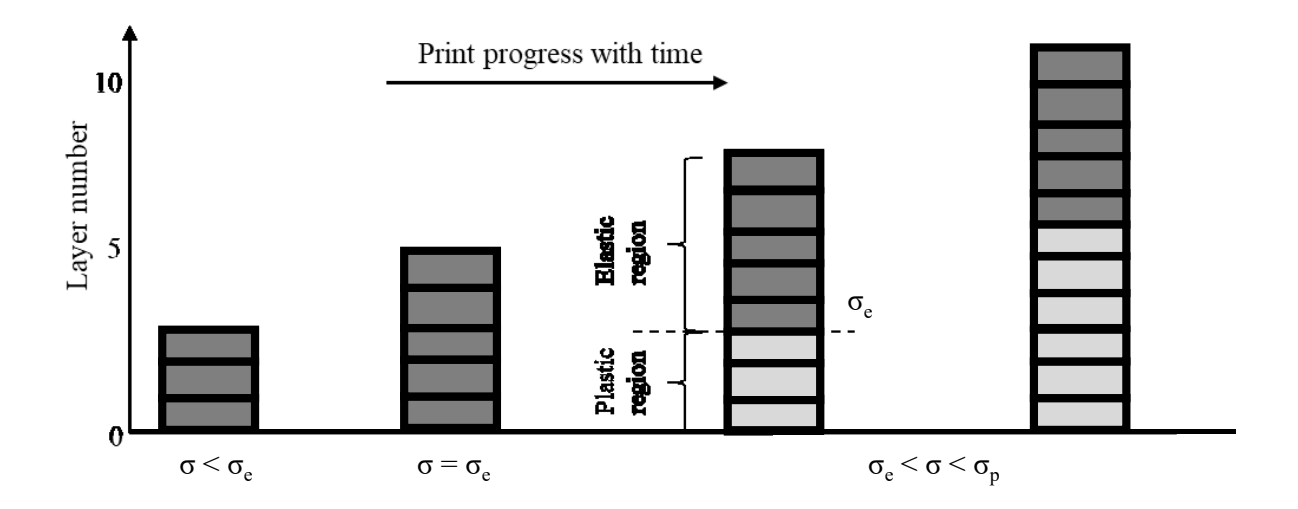


Figure 4: Schematic showing the layers experiencing stresses lower than the elastic yield stress (dark) and greater than the elastic yield stress (light); σ is the stress on the bottommost layer of the print.

2.3 Theoretical modes of failure

Several failure modes are at play, which decides the failure height during printing, depending on the state of the material based on the stress-strain relationship shown in Figure 2. These are elaborated in this section. First, it is possible that the failure is an elastic yield collapse wherein the stress exceeds the elastic yield stress. Modifying Eq. 1, the print height at which stresses on the lower filaments exceed elastic yield stress can be described as [21]:

$$h_e = \frac{\sigma_e}{\rho g}$$
 Eq. 2

where h_e is the elastic height limit, and σ_e is the elastic yield stress.

The printed structure could continue to absorb further load without visible structural failure even if a few bottom layers have exceeded their elastic yield stress limit. However, it might be possible, depending on the geometry and aspect ratio of the printed structure, that elastic buckling could occur even before reaching the elastic height limit (h_e) dictated by the previous condition. The height at which elastic buckling due to self-weight ($h_{b,el}$) occurs is given as [32] (Eq. (3)):

$$h_{b,el} = \left[7.8373 \frac{E_e I}{\rho \, qA}\right]^{\frac{1}{3}}$$
 Eq. 3

where E_e is the elastic modulus and I is the second moment of inertia. Note that this failure can occur only if the condition $h_{b,el} < h_e$ is satisfied.

As the print height exceeds h_e , with each additional printed layer at the top for a total height of h_{total} , a new layer in the bottom (at $h=h_{total}-h_e$) experiences a stress that exceeds the elastic stress limit as described in Figure 3. The progressively increasing number of layers in the plastic region will continue until the stress on the bottommost layer of the print reaches the plastic stress limit. At this point, the mode of failure is termed the plastic yield failure, and the corresponding height (h_p) is given by modifying Eq. 1 as [21]:

$$h_p = \frac{\sigma_p}{\rho a} + h_l$$
 Eq. 4

where σ_p is the plastic yield stress and h_l is the filament layer height. The layer height is added to indicate that the stress is being calculated at the top of the bottommost layer.

As shown in Figure 4, once the elastic stress limit is exceeded, the printed specimen is subjected to differing stresses at different levels, with the material on the top portion (recently printed) in the elastic regime, while a plastic regime exists in the bottom layers. Failure could occur in this transition stage before reaching the plastic yield stress under a combined failure condition. The system in this case is considered as an element with a plastic modulus (E_p) , that is subjected to an applied load which is equal to the selfweight of the elastic portion (layers on top subjected to stress $< \sigma_e$). The system is assumed to be in a fixed-free boundary condition, and the crippling length (l_{crip}) is thus given as [33]:

$$l_{crip} = \sqrt{\frac{\pi^2 E_p I}{4 \times \sigma_e A}}$$
 Eq. 5

Here, E_p is the plastic modulus and is defined in this work as the slope of the initial (linear) plastic stress-strain response regime shown in Figure 2.

Hence, the height of print at failure (h_{crip}) can be calculated as:

$$h_{crip} = l_{crip} + h_e$$
 Eq. 6

The failure can also be dictated by the self-buckling of the entire printed system, which is termed here as elasto-plastic buckling failure. Here, the material properties, except the modulus, can be assumed to remain constant along the print height. Given the two different moduli in the system - an elastic modulus (E_e) for the length of material stressed below the elastic yield stress limit, and a plastic modulus (E_p) for the material in layers subjected to stress > σ_e , the height of elasto-plastic buckling failure under selfweight $(h_{b,eff})$ is given as:

$$h_{b,eff} = \left[7.8373 \frac{E_{eff}I}{\rho qA}\right]^{\frac{1}{3}}$$
 Eq. 7

where E_{eff} is the combined modulus of the printed system, determined from the total vertical deflection under self-weight. A weighted mean approach shown in Eq. 8 is used to determine the effective elastic modulus of the printed structure.

$$E_{\text{eff}} = \frac{(h_e + h_{p,\text{eff}})^2 E_e E_p}{h_e^2 E_p + h_{p,\text{eff}}^2 E_e}$$
 Eq. 8

where $h_{p,eff}$ is the height of the printed portion that is in the plastic regime at the time of elasto-plastic buckling failure. Substituting E_{eff} in Eq. 7, and using $h_{b,eff} = h_e + h_{p,eff}$ as a necessary condition, Eq. 9 is obtained.

$$(h_e + h_{p,eff}) - \left[7.8373 \frac{E_e E_p I}{(h_e^2 E_p + h_{p,eff}^2 E_e) \rho g A}\right] = 0$$
 Eq. 9

The value of $h_{p,eff}$ is obtained by solving this equation. It can be easily seen that this equation does not have a solution if $h_{b,el} < h_e$, in which case the layer stresses are within the elastic yield limits.

Based on the above discussions on failure modes, four different modes of failure could occur during a print, i.e., elastic buckling, plastic yield, crippling and elasto-plastic buckling, and the respective failure heights can be calculated using Eq. 3, 4, 6, or 7. At any given point of time, the lowest predicted failure height is considered to be the expected print failure height.

3. Experimental Program

The experimental program consists of green compression test (GCT) on 3D printed mortar cylinders at different times after mixing, towards defining their material characteristics. Then using the material characteristics, failure heights are predicted using the model developed in Section 2. Further, 3D printing

of elements with two different geometries are carried out to determine the failure heights experimentally, to allow comparisons with the predicted values. Figure 5 is a concise representation of the entire approach outlined in this paper – the theoretical prediction of failure curves through the parameters derived from GCT, and the experimental validation of buildability (failure heights) using wall and hollow cylinder geometries. In addition, digital image correlation (DIC) was also used to extract deformations and strain rates as a function of layer addition to develop buildability indicators, which is the topic of a companion paper.

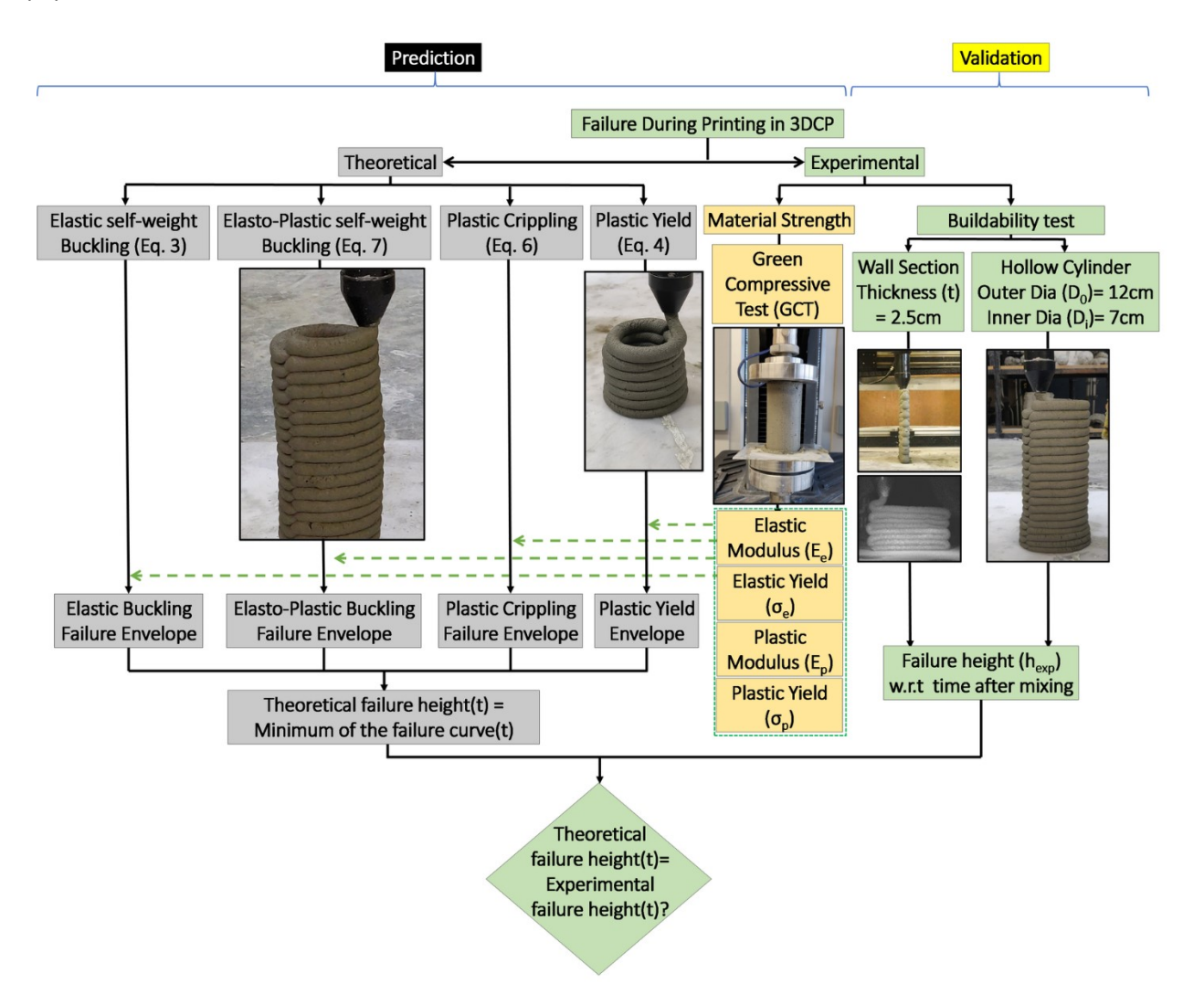


Figure 5: Theoretical prediction approaches for buildability prediction and their experimental verification.

3.1 Materials and mixtures

Mortar mixes were proportioned using a Type I/II cement conforming to ASTM C 150, fly ash conforming to ASTM C 618, and fine limestone powder of median size (d₅₀) 1.5 µm conforming to ASTM C 568. The cement-limestone mixtures used for 3D printing were developed in an earlier work by the authors, considering particle packing and rheological characteristics necessary for printability [34]. A polycarboxylate ether-based superplasticizer was used in some of the mixtures. The particle volume fractions in the paste component of the mortars ranged from 0.43 to 0.49. A commercial medium sand (Quikrete), conforming to ASTM C 778, with a median particle size of 0.5 mm, or a crushed expanded clay lightweight sand having a median particle size of 1.75 mm (size range 0.15 to 4.75 mm) provided by Arcosa Lightweight, conforming to ASTM C 330 and ASTM C 331, were used as the aggregates. Table 1 shows the chemical compositions of the materials used. The particle size distributions (PSD) of the materials used are shown in Figure 6. While several mixtures were proportioned to evaluate their buildability, details of only four mixtures are shown in Table 2 to ensure succinctness in discussions. Three mixtures use normal sand as the aggregate (identified as M), and one uses lightweight aggregate (identified as LWA in the table). The aggregate volume fraction is kept to 50% of the volume fraction of all the solids in the mixture, which results in significant differences in mass fractions of the ingredients between the normal weight and lightweight mixtures.

Table 1: Chemical composition of the mortar components

Components of the binders	Chemical composition (% by mass)							
	SiO ₂	Al_2O_3	Fe ₂ O ₃	CaO	MgO	SO ₃	LOI*	
OPC	19.60	4.09	3.39	63.21	3.37	3.17	2.54	
Fly Ash (F)	54.93	20.44	4.57	9.93	2.81	0.86	0.99	
Limestone (L), 1.5 μm	CaCO₃ > 99%							
Medium Sand (M), 0.6 mm	SiO ₂ > 99%							
Lightweight aggregate	62.68	17.79	7.37	4.10	3.01	0.75	0.03	
*Loss of Ignition								

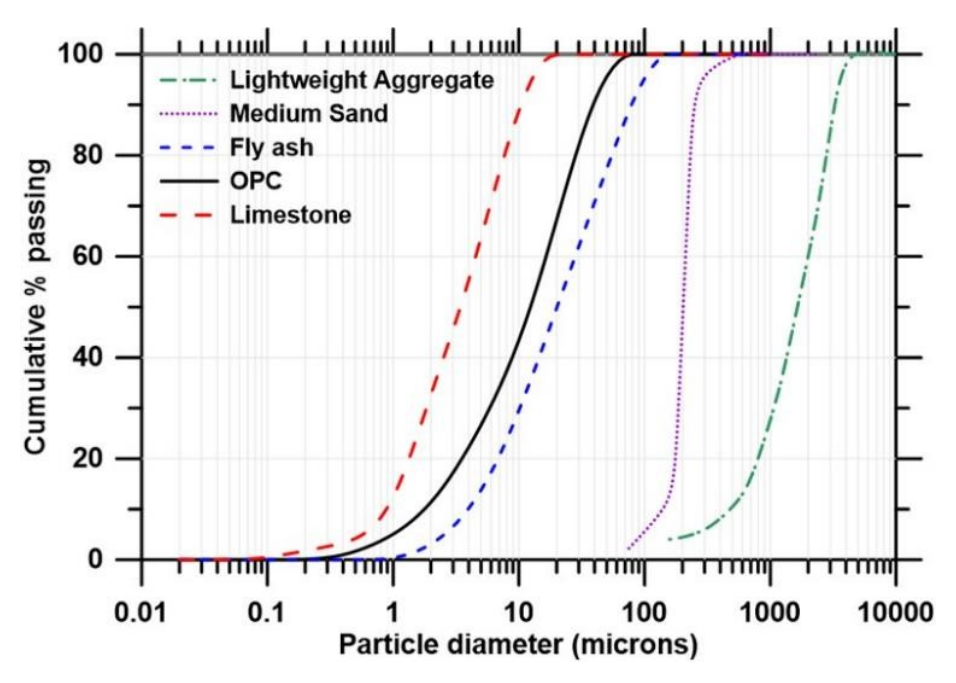


Figure 6: Particle Size Distribution of the mortar components

Table 2: Mortar mixture proportion used in the study

	Mass fraction of ingredients					Water-to-	SP to	Particle volume
Mixture	OPC	Limestone	Fly	Sand	LWA	binder ratio	powder	fraction in the
ID		(L;	Ash	(M)		(w/b) by	ratio (SP%)	paste phase
		d ₅₀ =1.5μm)	(F)			mass	by mass	
L _{30-M}	0.37	0.16	-	0.47	-	0.43	-	0.437
L _{30-S-M}	0.37	0.16	-	0.47	-	0.35	0.35	0.488
F ₂₀ L _{10-M}	0.36	0.05	0.10	0.49	-	0.37	-	0.491
L _{30-LWA}	0.49	0.21	-	-	0.30	0.35	0.25	0.488

3.2 Green Compression Test (GCT)

GCTs were conducted on fresh mortar cylinders 50 mm in diameter and 100 mm long, every 30 min from the time of mixing. Several preliminary tests brought out the need for a robust and efficient specimen preparation method to obtain accurate and repeatable GCT results. The printing of cuboids to obtain GCT samples and their extraction procedure are shown in Figure 7. A cuboid of size $80 \times 60 \times 120$ mm was printed on an acrylic plate, a few minutes before the GCT test time (7 minutes to be exact). Each layer consisted of three 20 mm wide and 80 mm long filaments, printed as shown in Figure 7(a). Flow rate was maintained such that the filaments overlap each other to avoid discontinuities at the vertical interfaces,

which was confirmed through visual observations of cut sections of the hardened specimens. A cylindrical steel tube 50 mm in inner diameter and 100 mm long was used to extract cylinders for GCT. One end of the tube was sharpened, and the inner surface lubricated to ensure that the tube cuts through the printed cuboid easily without deforming the specimen. The excess material outside the tube was removed, followed by leveling of the top surface of the specimen. Printing of cuboids and extraction of cylinders were repeated every 30 min until 2 h (generally) to generate a total of four specimen sets for each mortar mixture (see

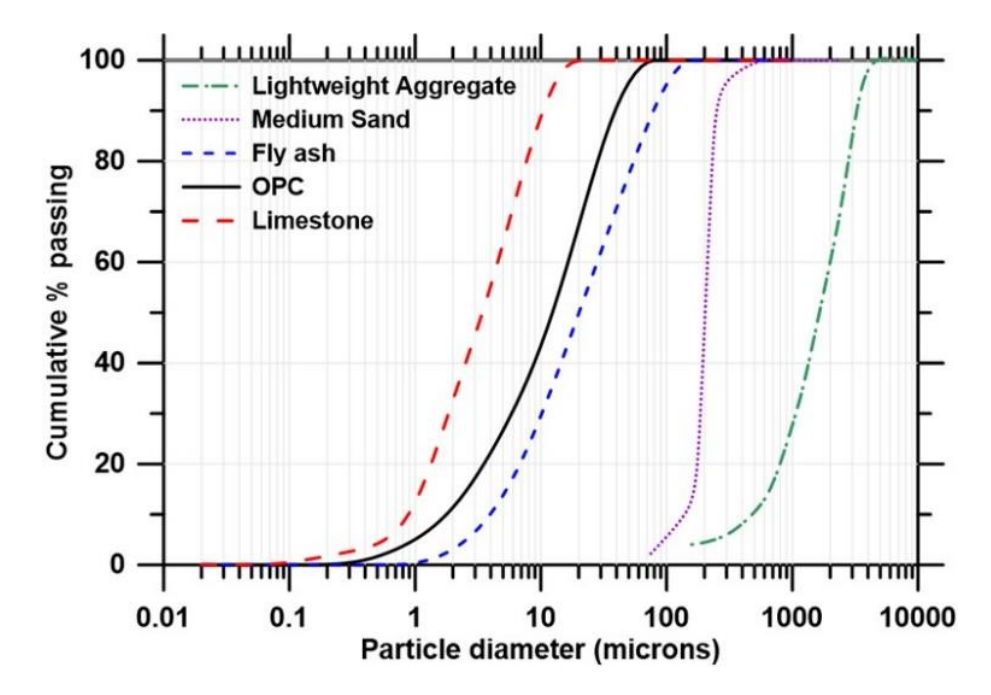


Figure 6: Particle Size Distribution of the mortar components

Table 2). Note that the printing time was 2 min, and the remaining 5 min were required to extract and prepare the sample for testing.

The extracted specimen with the tube was placed between the loading platens of a displacement-controlled testing machine (MTS Exceed Series 40 E42 with rated force capacity of 5 N-5 kN) and the tube was slowly removed to release the specimen in place. An acrylic plate (54 mm in diameter) was then placed on top of the specimen and rotated slightly without applying any vertical force to ensure proper contact. The top platen of the loading machine was slowly lowered to just touch the top surface, and then moved up to release the load. To ensure an even contact surface, the loading platen was lowered to move at 1 mm/min for a very short time, and then the load was released. Overall deformation caused in this process, to ensure a better contact surface, was usually less than 0.5 mm. Care was taken to ensure that

the contact surfaces were as flat as possible, and the specimen was concentrically placed with complete contact during testing, to avoid eccentric loading. The specimen was then left for a minute and then the test was started. A loading rate of 1 mm/min (corresponding to a strain rate of 0.01/min) was used to ensure that the loading rate in GCT was similar to that during the printing. This was chosen such that the total testing time is also not large enough to cause time-dependent effects to be dominant in the measured response. The small loading rate also allowed identification of the initial elastic and plastic regions in the stress-strain response. The compression tests were terminated at a total deformation of ~10 mm (~10% strain).

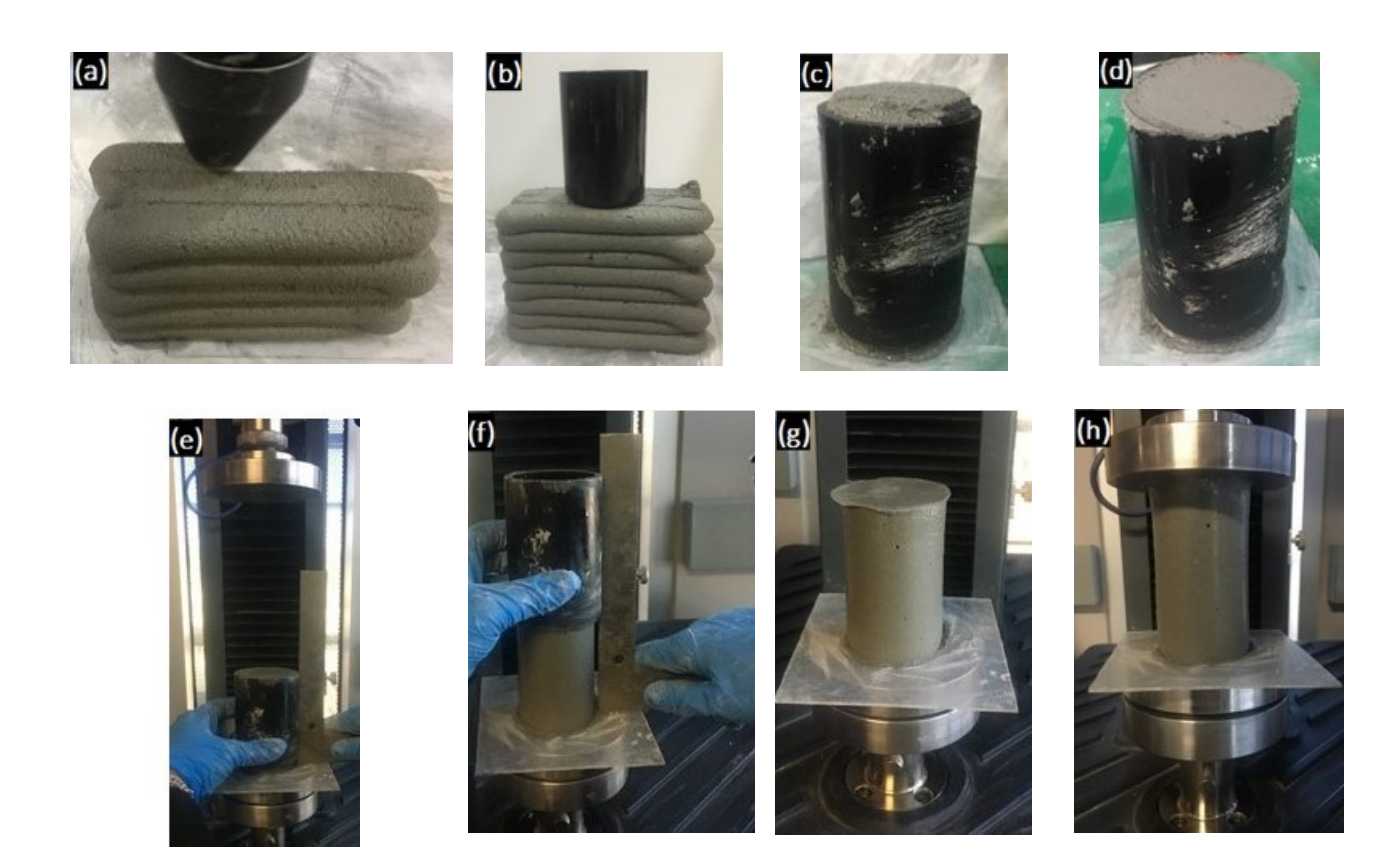


Figure 7: Sample preparation and green compression testing (GCT): (a) printing of the cuboid, (b) after printing and the metal tube ready to be inserted, (c) after inserting the tube and removing excess material from outside, (d) excess material removed from the top and leveled, (e) specimen with tube placed between the loading plates, (f) using an angle to carefully release the tube and align the specimen with the test setup, (g) placing an acrylic plate on the surface for a level contact surface, and (h) cylinder under testing.

3.3 Characterization of failure and prediction of failure curves

The material characteristics of the mortars (shown in Figure 2) were extracted from the engineering stress-strain plots recorded using the GCT carried out at regular intervals (0.5, 1, 1.5 and 2 h) after mixing. The elastic and plastic modulus (E_e and E_p) were extracted using linear fits in the elastic and initial plastic regimes respectively of the stress-strain curves as indicated in Figure 2. The average plastic modulus was estimated using linear fits in the initial plastic regime. The moduli were found to vary by approximately 5-10% if the fit range was extended all the way to the plastic yield point, due to the more evident non-linear stress-strain behavior when approaching the plastic yield point (also shown in Figure 2), as well as discrepancies in establishing the exact plastic yield point based on the rate of stress change with incremental strain. The elastic yield stress (σ_e) was identified as point of initial shift in linearity that demarcates the elastic and initial plastic regimes. The plastic yield stress (σ_p) was identified as the point of inflection (decreasing rate of change in slope) within the plastic regime. Using these values, failure heights were determined for each of the proposed failure modes as discussed earlier (Section 2.3). The minimum of these predicted failure heights at each of the test times forms the points on the expected time-dependent failure curve for a given mixture. This was verified using the actual print results as discussed in the forthcoming sections.

3.4 3D printing of mortars

The mixtures shown in Table 2 were printed using a gantry printer equipped with a screw extruder system (shown in Figure 8Error! Reference source not found.) and connected to a hopper to feed the material, and extruded through a circular nozzle of diameter (ND) 20 mm. A circular nozzle was used instead of a rectangular nozzle to obtain consistent filament cross-section for wall and cylinder prints; in other words, for non-orthogonal print paths, the layer width will not be consistent with a rectangular nozzle. Moreover, there was no degree of freedom for the nozzle in the printer.

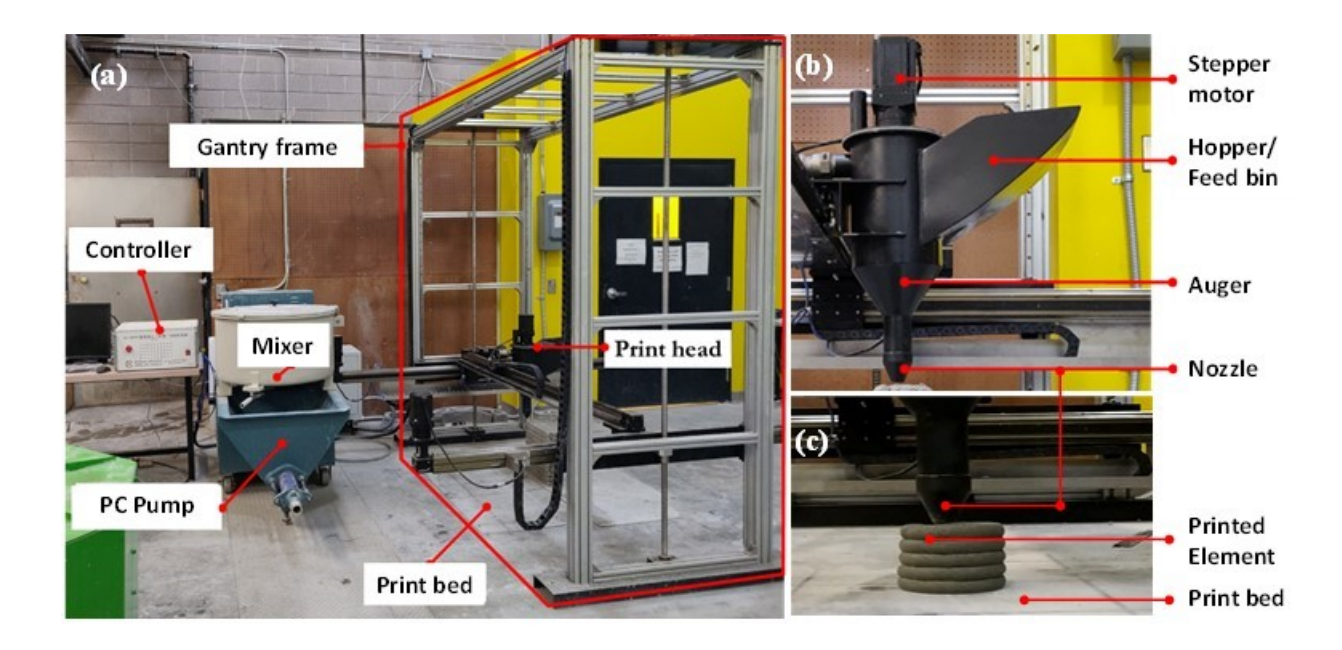


Figure 8: Printer setup showing: (a) the gantry printer with the controller and the mixer, (b) close-up of the print head, and (c) a cylinder print in progress.

The schematics of the selected designs are shown in Figure 9. A wall section 200 mm long × 25 mm wide was printed, at an in-plane print speed of 15 mm/s, and 5 mm/s in the vertical direction (z direction; the plane-changing speed), at an equivalent flow rate of about 5.63 mL/s. The circular hollow section was printed with an outside diameter of 120 mm and an inside diameter of 70 mm at a print speed of 25 mm/s in-plane, and 5 mm/s in the z-direction, and an equivalent flow rate of about 9.3 mL/s. The in-plane print speeds were different to ensure similar vertical printing rates for both the designs (for the walls, 3.67 layers/min, and for the hollow cylinders, 3.85 layers/min). The layer height chosen for print was 15 mm i.e., 0.75 times nozzle diameter to ensure that the layer is subjected to some vertical pressure to improve the interlayer bond, as discussed in our previous work [35]. The vertical pressure applied by nozzle during extrusion was experimentally calculated by printing filaments over a weighing balance and was determined to be in the range of 1.7 to 2.1 kPa. Printing was continued until the printed element showed unstable failure, and the corresponding height was recorded as the failure height. Prints were repeated every 15 min after mixing, starting at 30 min after mixing until 2 h, or when the mixture was no more extrudable. Extrudability is qualified here as the ability to extrude filaments of uniform size under a near constant auger speed, without visible signs of cracking or discontinuities during printing.

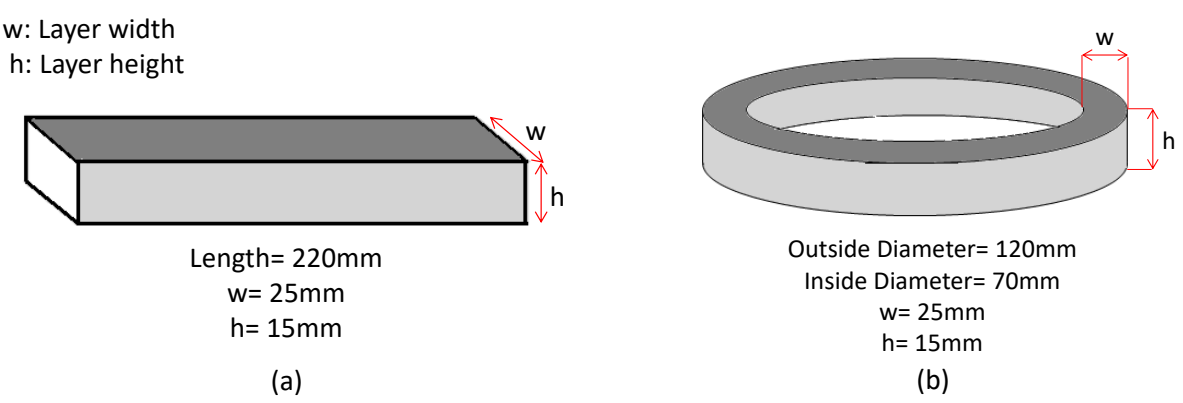


Figure 9: Details and dimensions for a single layer of: (a) wall print, and (b) hollow cylinder print

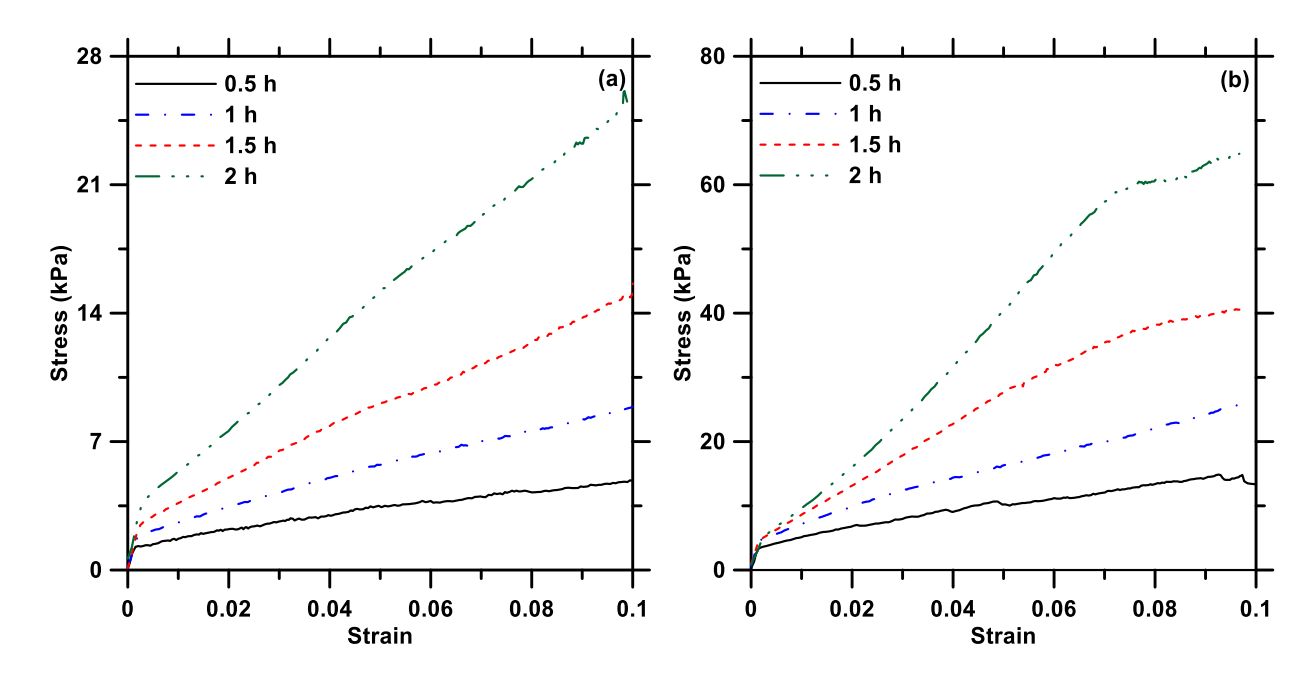
4. Results and Discussions

4.1 Green compression test (GCT) and extracted parameters

The stress-strain responses of cylinders printed at 30 min intervals after mixing (until 2 h) was obtained from GCT and are shown in Figure 10 for all the four mortar mixtures described in Table 2. These are representative responses, and replicate specimens showed very similar behavior, with a \pm 10% variation from the mean curves. Considering the bottommost layer 15 mm high in the cylinder, the stress on this layer caused by the self-weight of the GCT specimen was calculated to be around 1.8 kPa. Since this is very similar to the vertical pressure exerted by the nozzle (Section 3.4), both were omitted from further analysis. The stress values were corrected for the force exerted by the acrylic plate on which load was imposed during the test. The elastic modulus (E_e), elastic yield stress (σ_e), plastic modulus (E_p), and plastic yield stress (σ_p) were obtained from the stress-strain responses shown in Figure 10 for different times, based on the methodology presented in Figure 2, and are shown in Table 3. It is clearly seen that GCT carried out based on the careful procedure described earlier is able to distinguish between the elastic and the initial plastic regimes which forms the basis for the bi-linear response model in the theoretical formulation. The relatively low strain rate used in this work is found to be beneficial in bringing out the very early elastic response.

For all the specimens studied here, the separation between the elastic and plastic response is generally observed at a strain value equal to lower than 0.0025, for all the testing times evaluated. Similarly, the plastic yield point is generally identified between a strain of 0.02 and 0.05 (plastic yield occurs at higher strains with time as the material stiffens, which is expected). In cases where the distinction between initial and secondary plastic regimes which defines the plastic yield point cannot be identified with accuracy, especially in the case of mixtures at later times (1.5-2 h), the rate of change of stress with strain is used,

as shown in Figure 11. The experimental data for two mixtures is shown to explain the approach. It is easy to demarcate the elastic yield point from this figure, where the initial rapid drop in the rate of stress starts. The stress corresponding to the transition point where an almost flat curve starts to drop is taken as the plastic yield point, which is identified in Figure 11. The slope of the rate of change in stress curve for the L_{30-M} mixture at 2 h initially increases slightly in the plastic response region as the strain increases, and then starts decreasing at a strain of around 0.04, and the corresponding stress value (13.08 kPa) is taken as the plastic yield stress. Similarly, for the L_{30-S-M} mixture at 1.5 h, the slope decreases around a strain of 0.044, and the corresponding stress value (25.04 kPa) is taken as the plastic yield stress. It was also noticed that, at strains near the points of slope change as shown in this figure, shear cracks started appearing on the outside surface of the specimen subjected to GCT, which also indicates the initiation of failure.



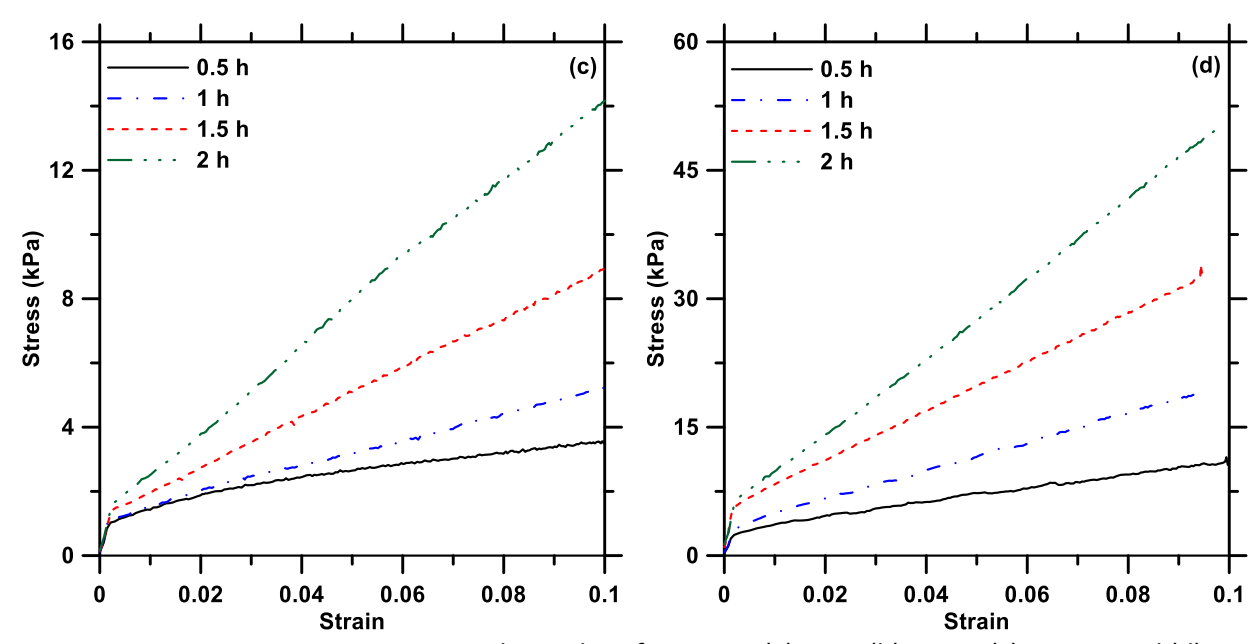


Figure 10: Representative stress-strain relationships from GCT: (a) L_{30-M} , (b) L_{30-S-M} , (c) $F_{20}L_{10-M}$ and (d) L_{30-L} mixtures. Note that the stress axis values are different for different mixtures.

Table 3: The mean elastic and plastic properties of the mortars extracted from the GCT results. The variability among the values is in the range of ± 10 -20%, which is expected in very early-age tests. Since time-dependency is of importance, focus is placed on the development of these properties, the trends for which can be accurately obtained from these tests.

Mixture ID	Time	E	lastic	Plastic		
	(h)	Yield stress (kPa)	Modulus (MPa)	Yield stress (kPa)	Modulus (MPa)	
L _{30-M}	0.5	1.21	0.99	2.28	0.056	
	1.0	1.65	1.03	3.58	0.088	
	1.5	2.56	1.14	6.74	0.14	
	2.0	3.71	1.47	13.10	0.22	
L _{30-S-M}	0.5	3.49	2.51	6.00	0.19	
	1.0	4.54	3.68	9.70	0.30	
	1.5	4.62	3.66	25.00	0.45	
	2.0	4.94	2.36	48.10	0.60	
F ₂₀ L _{10-M}	0.5	1.06	0.57	1.98	0.047	
	1.0	1.06	0.69	2.20	0.055	
	1.5	1.38	0.64	3.91	0.074	
	2.0	1.61	0.68	6.57	0.12	
L _{30-LWA}	0.5	2.49	1.49	4.10	0.14	
	1.0	3.33	1.63	6.05	0.20	
	1.5	5.77	3.60	16.70	0.30	
	2.0	6.58	3.19	27.70	0.41	

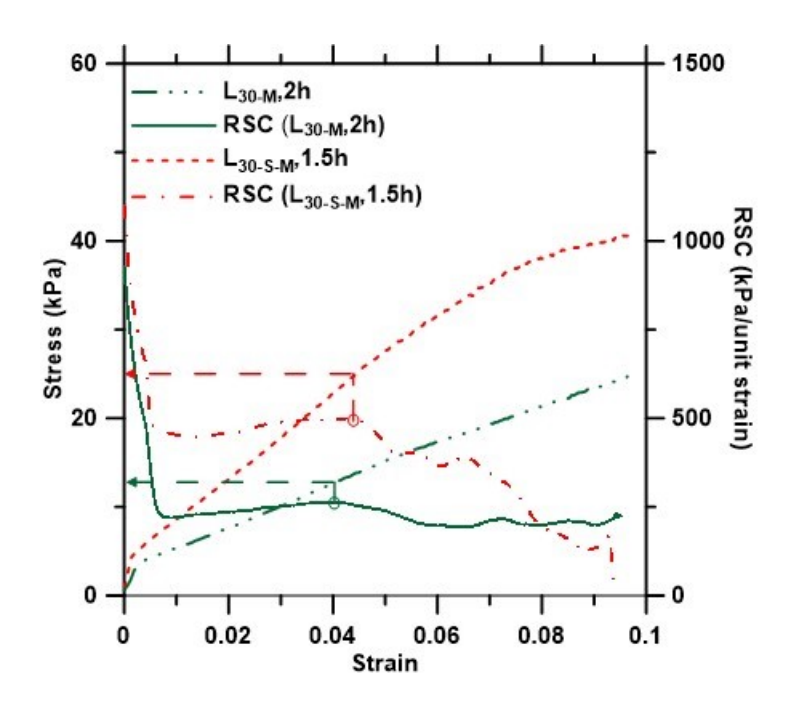


Figure 11: The use of rate of stress change (RSC) with strain to identify the plastic yield stress for mixtures especially at later times.

4.2 Time-dependence of yield stresses for different mixtures

Figures 10(a)-(d) and Table 3 indicate that the elastic and plastic yield stress values are significantly different between the mixtures. For instance, the stresses in the fly ash-containing mixture is lower than those in the other mixtures, likely attributed to the enhanced consistency of this mixture and the lack of particle interlock due to the spherical fly ash particles that facilitate reduced resistance to deformation [36]. This effect is more apparent when the later-age response of this mixture (with a w/p of 0.37) as shown in Figure 10(c) is compared to that of an OPC-limestone mortar (Figure 10(a)) proportioned using a higher w/p (of 0.43). The stresses are higher in the latter case, even when the w/p is higher.

The time-dependence of change in yield stress (typically used for static, shear yield stress) is described by the structuration rate [37]. For a short period of time after mixing, the yield stress growth for a mixture can be assumed to be linear. This usually is the case during the dormant period prior to setting [38,39]. The shear yield stress increases exponentially with time [40]. Perrot et.al. [37] proposed an exponential yield stress-based structuration rate calculation. Such an approach, with some modifications, is used here for quantifying time-dependence of stresses obtained from GCT. The shear yield stress at time t, $\tau_0(t)$ is described as [37]:

$$\tau_0(t) = A_{thix} t_c \left(e^{\frac{t}{t_c}} - 1 \right) + \tau_{0,0}$$
 Eq. 10

where, $\tau_{0,0}$ is the yield stress at time t=0, and A_{thix} is the structuration rate which is obtained by adjusting the value of characteristic time t_c to obtain the best fit using the shear stress growth data.

The plastic yield stress (σ_p) obtained from GCT can be considered to be related to the shear yield stress of the deposited material (in a manner similar to how extrusional and shear yield stresses are related), and therefore can be expressed as [16]:

$$\sigma_n(t) = \alpha_{geom} \cdot \tau_0(t)$$
 Eq. 11

where, α_{geom} is a time-independent factor which depends only on the geometry of the printed structure. Eq. 11 can then be substituted in Eq. 10 to obtain the structuration rate in terms of plastic yield stress rather than the shear yield stress typically determined using rotational rheology.

$$\frac{\sigma_p(t)}{\alpha_{geom}} = A_{thix} t_c \left(e^{\frac{t}{t_c}} - 1 \right) + \frac{\sigma_{p,0}}{\alpha_{geom}}$$
 Eq. 12

$$\sigma_p(t) = \alpha_{geom} A_{thix} t_c \left(e^{\frac{t}{t_c}} - 1 \right) + \sigma_{p,0}$$
 Eq. 13

For a given fixed print cross-section, the structuration rate between different materials can then simply be compared by comparing $\alpha_{geom}A_{thix}$ since α_{geom} is a constant. Replacing $\alpha_{geom}A_{thix}$ by A_{thix}^* ,

$$\sigma_0(t) = A_{thix}^* t_c \left(e^{\frac{t}{t_c}} - 1 \right) + \sigma_{p,0}$$
 Eq. 14

 $\sigma_{p,0}$ is hard to determine experimentally since testing cannot be started right away after mixing. Exponential fit was used for the GCT results at 0.5, 1, 1.5 and 2 h, and then extrapolated backwards to time t=0 to obtain $\sigma_{p,0}$.

Figure 12 shows the variation of plastic yield stress with time, and the modified structuration rates of the tested mixtures. It can be seen that A_{thix}^* of the L_{30-M} mixture is higher than that of the F₂₀L_{10-M} mixture, despite having a reduced particle packing (as shown in Table 2) than the fly ash-containing mortar mixture. In contrast, the strength and stiffness of the L_{30-S-M} mixture is 2.5 to 3 times that of the non-superplasticized counterpart, while the structuration rate is found to be about 2.77 times, showing the correspondence between the structuration rate and strength or stiffness development, both of which are functions of time-dependent microstructure development. The improved particle packing imparts a higher structuration rate [41] to the superplasticized mixture with a lower w/p, and the faster strength development allows better buildability. However, this could result in a shorter printability window since

the faster strength development could hinder adequate extrusion at later times, which could be controlled using additives/admixtures [42,43]. The superplasticized mortar, L_{30-S-M} shows a much higher structuration rate than the non-superplasticized counterpart because of the lower w/p and increased packing fraction in the paste. In fact, the importance of particle packing is 3D printing is brought out here, where a structuration rate three times higher is obtained by simply making minor changes to the mixture.

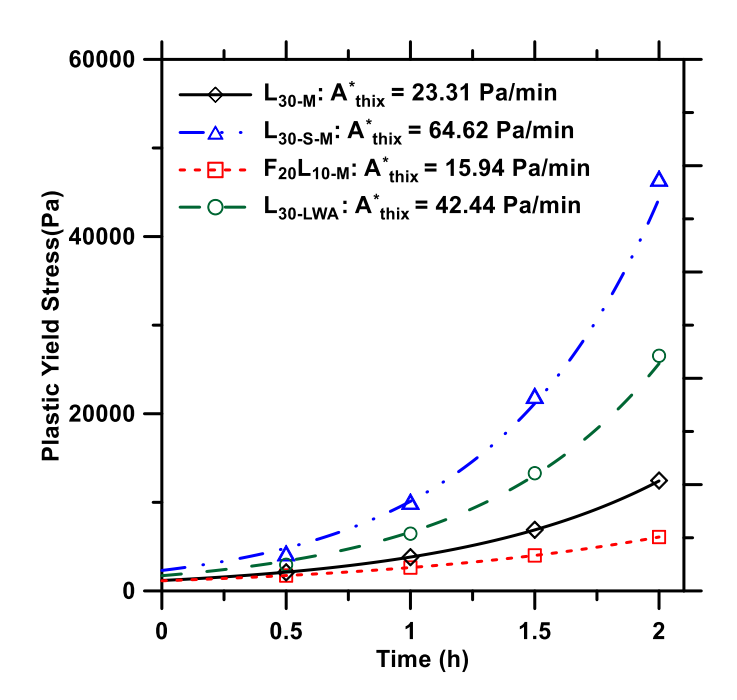


Figure 12: Plastic yield stress as a function of time to determine the modified structuration parameter A_{thix}^* for different mixtures

4.3 Verification of theoretical failure height curves using wall and cylinder printed elements

The failure heights of the printed wall and cylindrical structures as a function of time $(h_{exp}(t))$ were recorded for all the chosen mortars. Failure is defined when no more layers could be printed because of significant geometric deformation and/or collapse of the printed structure. These results are compared with the failure curves derived based on the analytical model as described in Section 2 and are shown in **Error! Reference source not found.** Figures 13-16. Wall and hollow cylindrical prints were made every 15 min until 2 h, while the theoretical failure curves are derived from GCT carried out at 30 min intervals until 2 h. The subfigures (a) and (b) in Figures 13-16 correspond to the experimental results and the theoretical predictions based on whether the printed structure is a wall or a hollow cylinder, respectively. Note that, for the L_{30-S-M} mixture, the printing could be done only until 1.5 h from mixing, as the mixture became too stiff and could not be printed continuously. The remaining three mixtures, L_{30-M}, F₂₀L_{10-M} and L_{30-LWA} were

still printable at 2 h even though in some cases, the lower layers showed minor cracking because of drying, which points to the need for improved curing practices.

Wall prints: Figures 13(a)-16(a) show the results for the wall sections printed using different mixtures. The failure heights $h_{exp}(t)$ (denoted by filled circles in these figures) obtained at different times are plotted along with the predicted failure curves attributed to plastic yielding, crippling, and buckling $\{h_p(t),$ $h_{crip}(t)$ and $h_{b,eff}(t)$ } obtained from Eq. 4, 6, and 7 respectively. It was found that for all the mixtures used in this study, the buckling height considering the elastic modulus alone was always greater than elastic yield limit height i.e., $h_{b.el}(t) > h_e(t)$, and thus Eq. 3 is not used in the development of failure curves. The failure heights, $h_{exp}(t)$, are found to be in reasonably good agreement with the lowest failure curve among the three predicted time-dependent failure curves. From these figures, it is also noticed that the failure of the walls at early times, i.e., printed after 30 min of mixing are reasonably well-predicted by all the failure mechanisms, though minor variations can be noted based on the mixture type. At later times, the experimental wall failure heights are closely approximated by the buckling/crippling curves as can be noticed from these figures. For the L_{30-M} mixture (Figure 13(a)), it can be seen that the wall print failure height at 0.5 h corresponds to the plastic failure prediction, and then closely follows the crippling failure curve beyond 0.75 h. The L_{30-S-M} mixture is stiffer than the L_{30-M} mixture and thus allows for a higher failure height (Figure 14(a)). The failure heights observed generally follow the lowest mode of failure (crippling) although it is slightly higher than the predictions at later times. The failure heights for the F₂₀L₁₀₋ M mixture shown in Figure 15(a) are similar to those of the L_{30-M} mixture, with critical failure heights around 100 mm initially with a further increase of around 50 mm in 2 hours, which is in line with the GCT results showing the slow stiffness gain due to the presence of fly ash on structural build-up, as reported elsewhere [36]. Similarly, the failure heights of the L_{30-LWA} mixture shown in 16(a) follows the buckling/crippling failure curve with time. When extrapolated to comparable geometries used in studies elsewhere [44,45], the wall failure heights obtained in this work are comparable. For example, failure at 22 layers corresponding to a height of 202 mm is reported in [44] for a wall of length 800 mm and width 43.5 mm. Wolfs and Suiker [45] printed three different lengths of 60 mm thick wall to change the print times and introduce curing effect on already printed filaments. For 1 m, 5 m and 10.4 m long walls, failure occurred after 21, 27 and 46 layers respectively, corresponding to heights of 199.5 mm, 256.5 mm, and 437 mm, respectively. The times taken for printing were reported to be 3.5 min, 21.6 min, and 76.5 min, respectively. Note that visual inspections were also carried out during printing to evaluate if the failure occurred due to slight out of plane movement (buckling) or vertical collapse (plastic yield). Based on

general observations during the printing, it can be stated that, for the wall prints, out-of-plane movement caused the final failure. Wall print at 30 min for L_{30-M} and $F_{20}L_{10-M}$ mixtures, however on careful inspection, showed a vertical squeezing of first layer which instantaneously made the print unstable. This instability results in a visual sense of failure due to out of plane movement. Figures 17(a)-(c) shows the images just at the time of failure of walls made using L_{30-M} mortar, printed at 45, 60, and 75 min after mixing. It was noticed that the print failure was immediately preceded by an out-of-plane movement, which is in line with the crippling mode of failure for these prints.

For wall prints, the failure heights predicted by the buckling/crippling curves are lower than the plastic yield failure for nearly all the print times. The plastic failure curve is independent of the print geometry, and scales simply with the time-dependent plastic yield stress development. On the other hand, the buckling/crippling failure curves are dependent on the geometry of the section (moment of inertia), along with the modulus. For a given mixture, any change in the modulus will be reflected in the plastic yield stresses also. Hence, to alter the buckling/crippling failure envelopes, while keeping plastic yield failure envelope constant, a section with higher moment of inertia than that of wall section is needed, which the hollow cylinders satisfy, the results for which are shown below.

Cylinder prints: Hollow cylinders as described in Section 3.4 were printed and the failure heights are shown in Figures 13(b)-16(b). As expected, the failure heights are much higher than those of the wall prints. At early times, the crippling and buckling failure models predict larger failure heights than the plastic yield collapse model, while the plastic collapse height predictions are generally higher than those for buckling and crippling at later times. At early ages (e.g., 30 min after mixing), the hollow cylinder prints were clearly found to subside vertically, which is in line with the plastic collapse mode, which was the lowest mode of failure predicted at these times. For the L_{30-M} mixture, Figure 13(b) generally indicates the plastic collapse mechanism to be dominant for the cylinder print at almost all times, while no failure mechanism is dominant as per predictions at 2 h. This is shown in Figures 17(d)-(f) that shows the failure point of L_{30-M} hollow cylinders printed at 45, 60, and 75 min after mixing. It can be clearly noticed that the lowest layer has undergone very high deformations at the point of failure. This is in line with the prediction of plastic yield collapse for this mixture. Hollow cylinders being more stable structures, some of the prints under plastic collapse subsided substantially but did not topple over. Since the structure did lose its geometric integrity in this case, it was considered to have failed. For the F₂₀L_{10-M} mixture shown in Figure 15 (b)), once again, plastic collapse is the dominant failure mechanism, which is accurately predicted by the model. For the other two mixtures shown in Figures 14(b) and 16(b), the failure modes change with time, and a cross-over is noticed. Moreover, at the transition points between the multiple failure mechanisms, the experimental cylinder print failure heights are generally lower than the theoretical predictions. This is likely attributed to the combined effects of multiple failure modes, causing premature failure. The experimental failure heights at 1.5 h for L_{30-S-M} and 2 h for L_{30-LWA} mixtures are higher than the predicted values, possibly because of the stiffness gain in the lower filaments during the longer time taken to complete the printing. Like wall print results, the cylinder print results are also in line with results reported elsewhere [24,25].

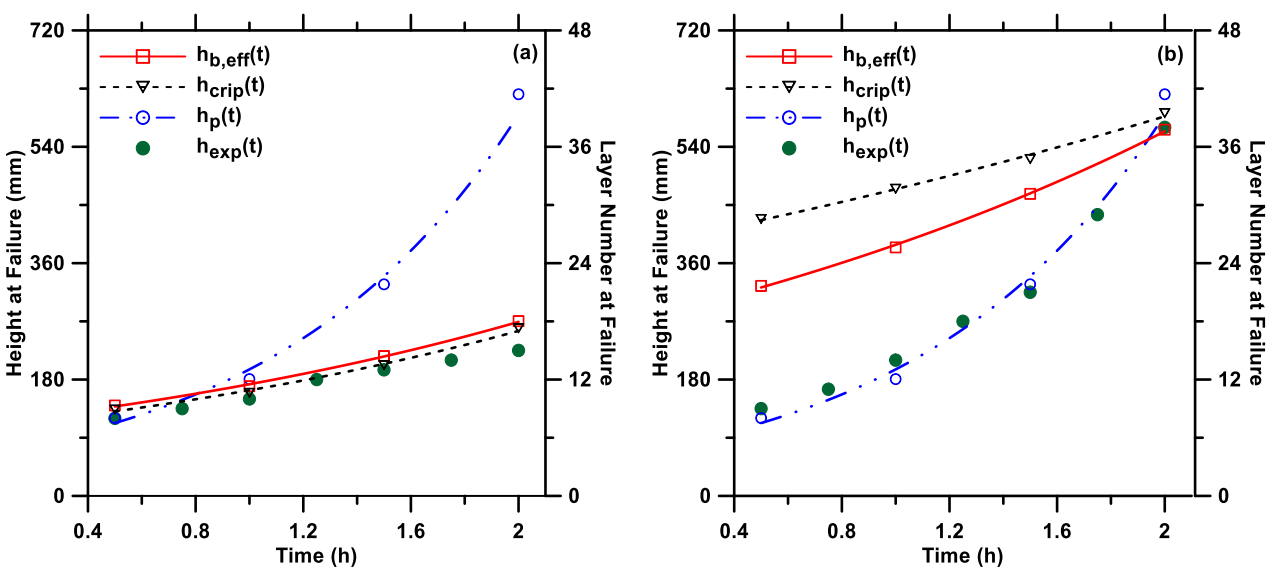


Figure 13: Comparison of experimental failure heights $(h_{exp}(t))$ with theoretical failure curves for buckling $(h_{b,eff}(t))$, crippling $(h_{crip}(t))$, and plastic yield $(h_p(t))$ failures for L_{30-M} mixture in: (a) wall print, and (b) hollow cylinder print

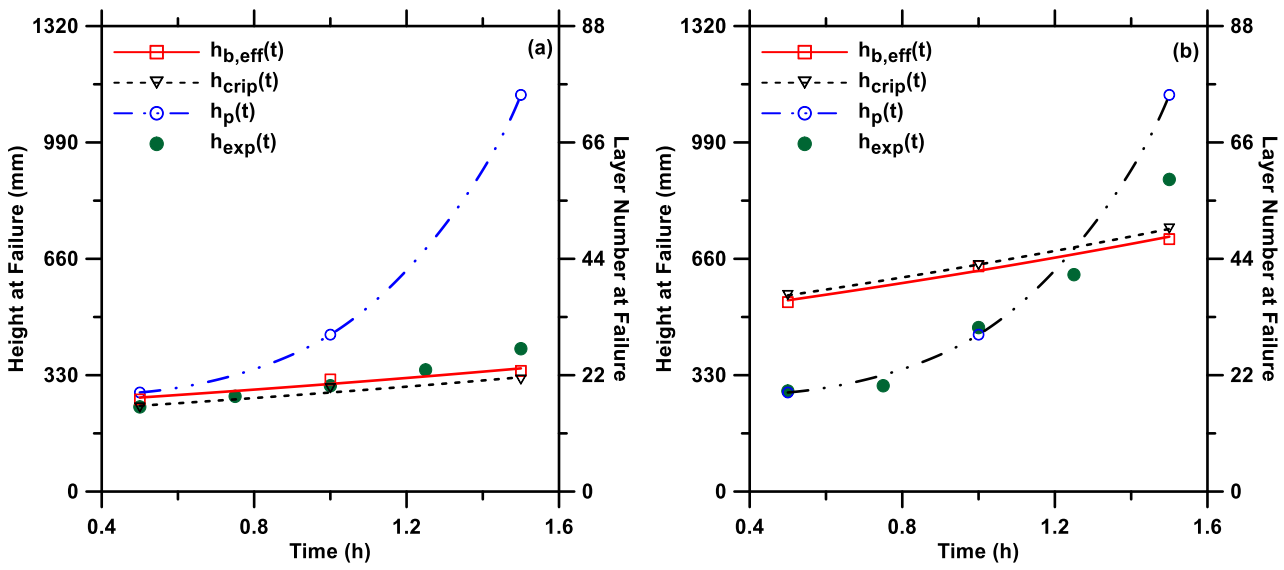


Figure 14: Comparison of experimental failure heights $(h_{exp}(t))$ with theoretical failure curves for buckling $(h_{b,eff}(t))$, crippling $(h_{crip}(t))$, and plastic yield $(h_p(t))$ failures for L_{30-S-M} mixture in: (a) wall print, and (b) hollow cylinder print

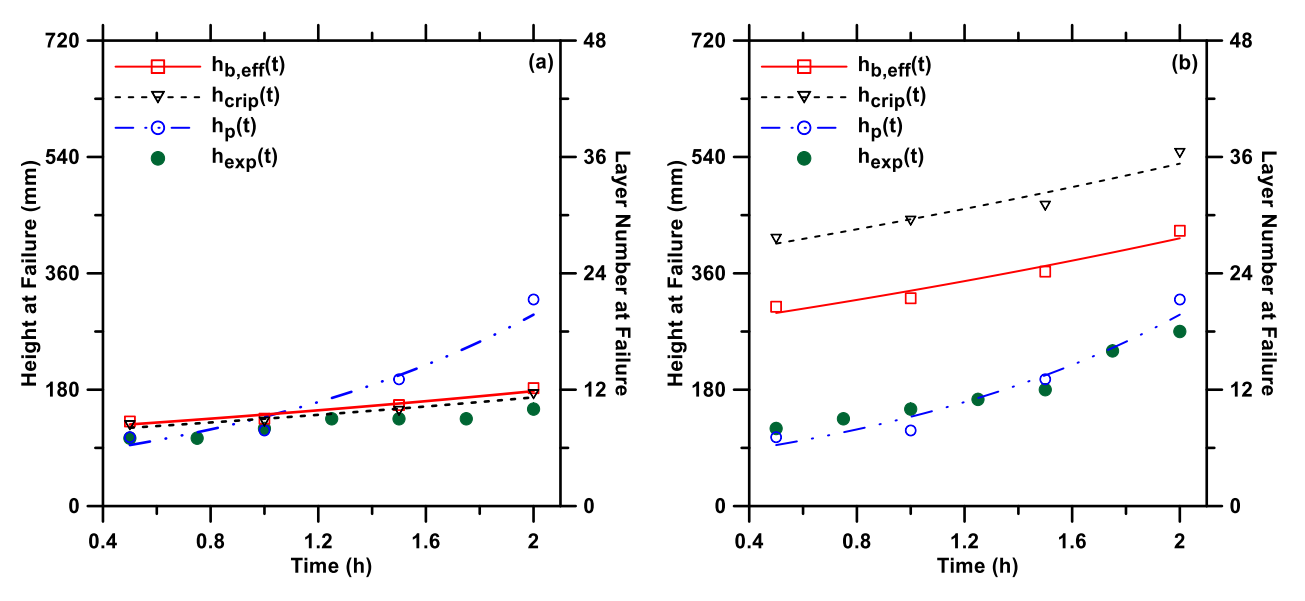


Figure 15: Comparison of experimental failure heights $(h_{exp}(t))$ with theoretical failure curves for buckling $(h_{b,eff}(t))$, crippling $(h_{crip}(t))$, and plastic yield $(h_p(t))$ failures for $F_{20}L_{10-M}$ mixture in: (a) wall print, and (b) hollow cylinder print

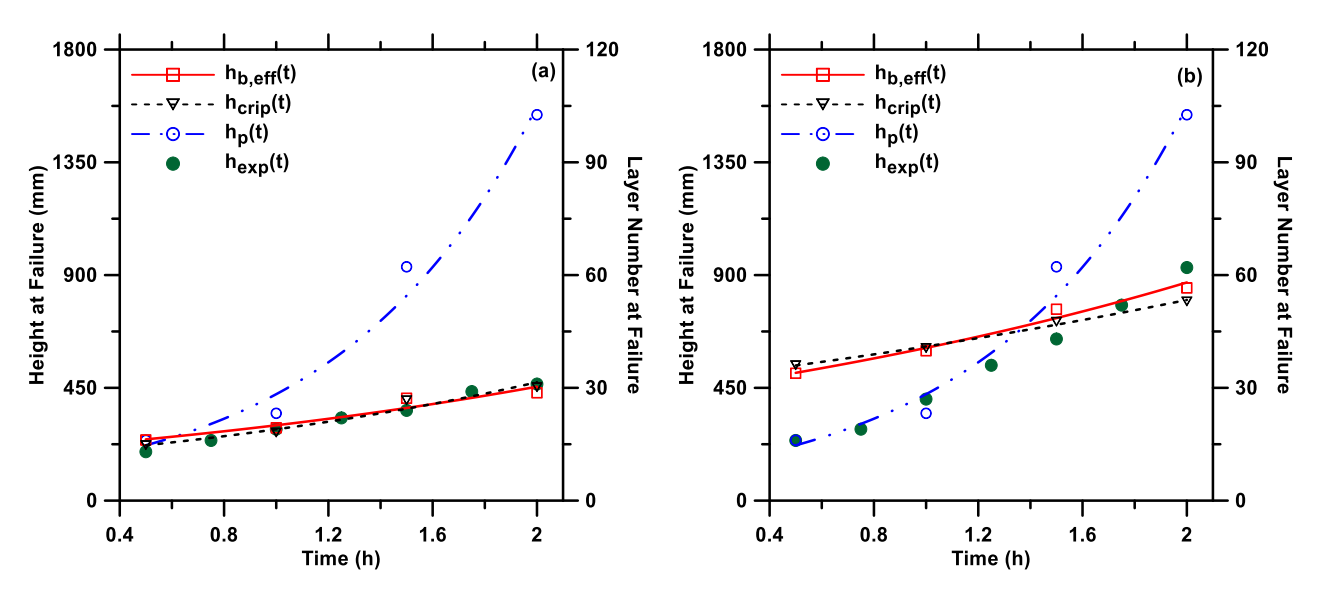


Figure 16: Comparison of experimental failure heights $(h_{exp}(t))$ with theoretical failure curves for buckling $(h_{b,eff}(t))$, crippling $(h_{crip}(t))$, and plastic yield $(h_p(t))$ failures for L_{30-LWA} mixture in: (a) wall print, and (b) hollow cylinder print

Figure 18 shows the mean absolute percentage error between the theoretical predictions and the experimental failure heights for all the mixtures. When evaluating an individual mixture and a print time, the predictions were mostly within ±15% of the experimental values. These differences could be attributed to the fact that the model does not apply any correction for geometrical and material imperfections (filament defects) induced by the printing process, and drying of the printed filaments caused by surface exposure and longer print times [44].

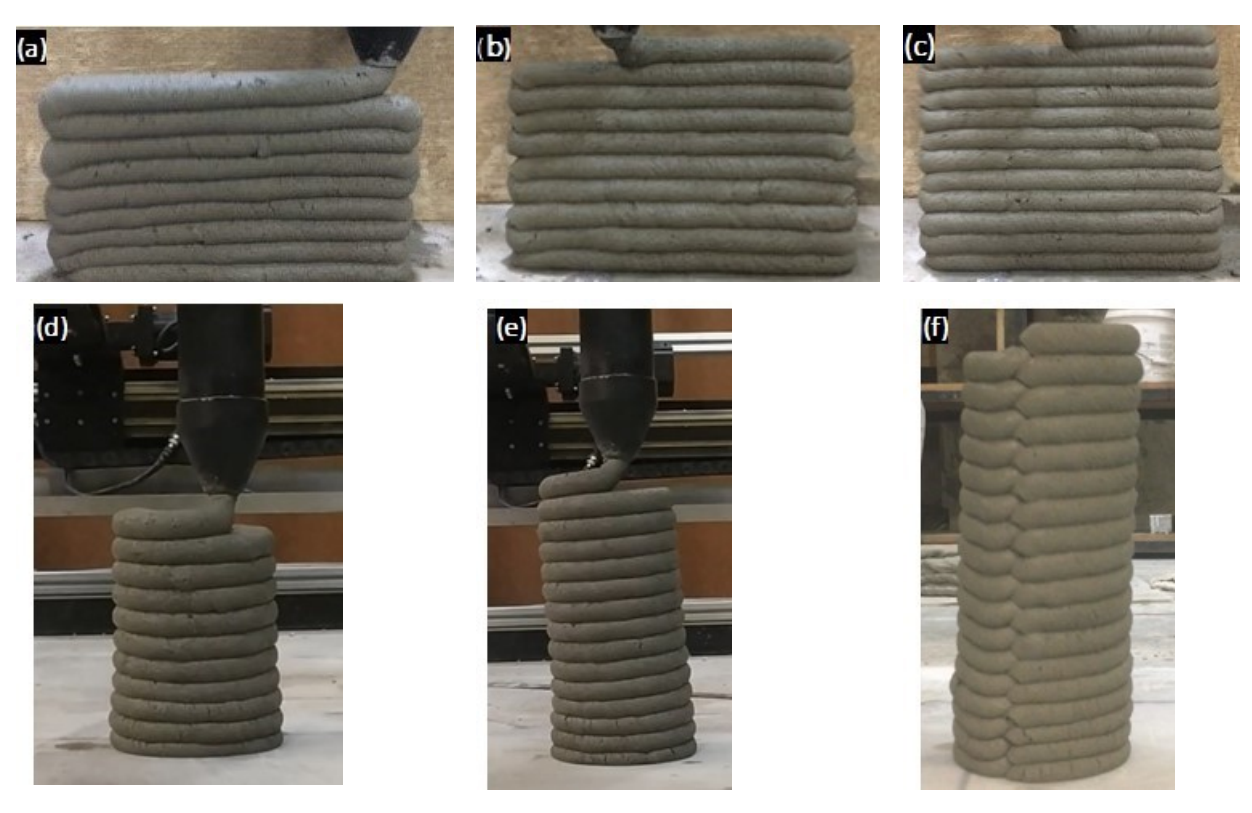


Figure 17: Wall prints at: (a) 45 min, (b) 60 min, and (c) 75min; and hollow cylinder print at: (d) 45 min, (e) 60 min, and (f) 75 min, at the instance of failure for the L_{30-M} mixture.

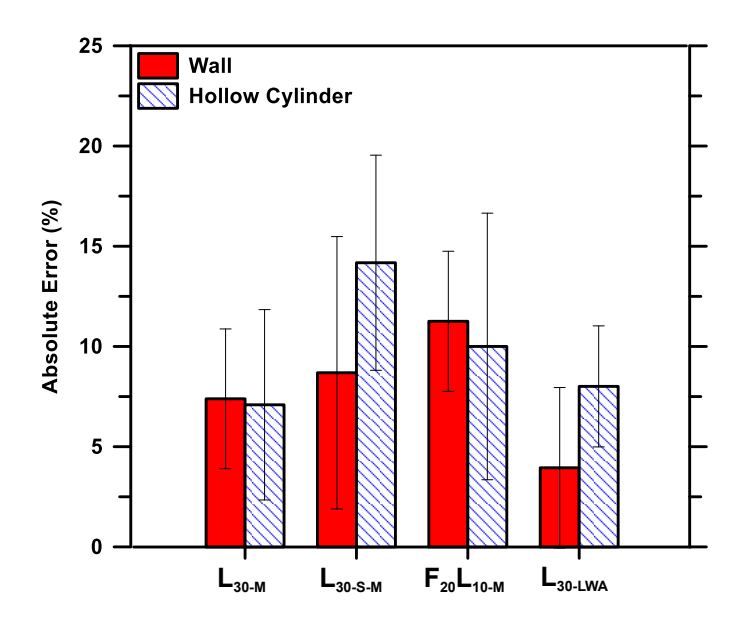


Figure 18: Average absolute error in prediction w.r.t experimental results for all four mixtures. The error bars indicate the spread in the error between predictions and measurements for all times tested.

The maximum experimental print height attained for the wall sections for the L_{30-M}, L_{30-S-M}, F₂₀L_{10-M} and L_{30-M} LWA mixtures were 225 mm, 405 mm, 150 mm, and 465 mm, respectively (Figures 13(a)-16(a)). These results were for a wall of width 25 mm, while in real-world printing, the wall thickness used can go up to 100 mm. In such cases, the walls could be printed as double-wythe structures with a hollow cavity in the middle as well, thereby changing some of the predictions in this work because of changes in geometry) which rely on solid walls. Figure 19(a) shows the theoretical failure curves for all the mixtures used in this study, when a solid wall of 100 mm thickness is printed. The theoretical curves are obtained by combining the relevant failure modes at different times shown in Figures 13-16 (using Eq. 4, 6, 7); thus, kinks in the theoretical curves are noted at times where the failure mode changes. The curves shown in Figure 19(a) represent the lowest mode of failure at any given time. The predictions for maximum failure height for the four mixtures increase to 514 mm, 649 mm, 320 mm, and 722 mm, respectively. Similarly, the maximum experimental print height attained for the 25 mm thick hollow cylinder section (external dia. 120 mm and internal dia. 70 mm) for the L_{30-M}, L_{30-S-M}, F₂₀L_{10-M} and L_{30-LWA} mixtures were 570 mm, 885 mm, 270 mm, and 930 mm respectively (Figures 13(b)-16(b)). Figure 19(b) shows the theoretical failure curve for 100 mm thick hollow cylinder specimens (external dia. 270 mm and internal dia. 70 mm). In this case, except for the L_{30-LWA} mixture, the failure curves for all the other mixtures are dominated by plastic yield collapse. The prediction for maximum print failure height for these mixtures, for the chosen geometry were 621 mm, 1125 mm, 320 mm, and 1202 mm, respectively.

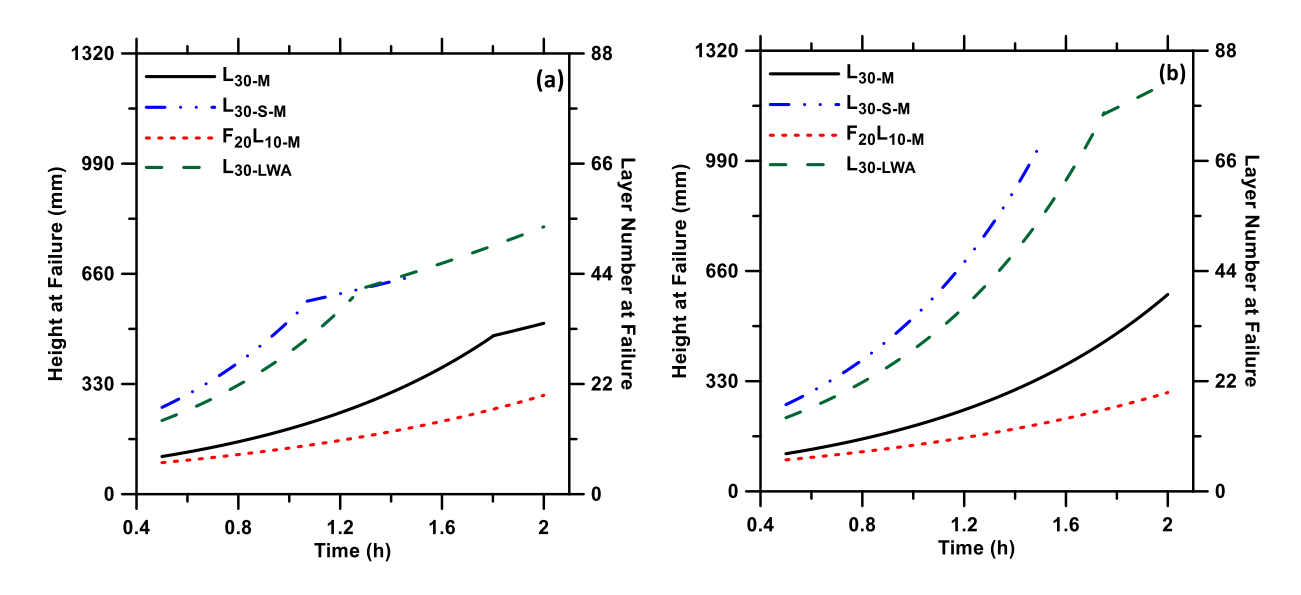


Figure 19: Theoretical failure height curves for (a) 100 mm thick wall, and (b) hollow cylinder(external dia. 270 mm, internal dia. 70 mm). Note that the lowest among the failure predictions are used at different times, and thus the shape of the curve changes as well.

5. Summary and Conclusions

The major objective of this study was to develop a model based on different potential failure modes for the buildability of 3D printed concrete at different times, and evaluate its applicability using experiments. The failure modes were dictated by the material characteristics and stress development in the built-up layers. The material characteristics were evaluated using carefully controlled green compression tests (GCT) on 3D printed cylinders extracted from prisms, while stress growth during layer build-up was determined from the material density and geometry of the layers. The tests were carried out at different times after mixing, up to 2 h, while ignoring the minor changes that could have occurred in the material properties during the duration of the printing process.

In the models used here, the material properties extracted from GCT are of special significance. GCT was carried out with modifications in the specimen preparation procedure (i.e., printing and extracting cylinders instead of casting cylinders, since the latter misrepresents the compaction levels and leads to erroneous properties) and loading rates such that the elastic response at very small strains, which is encountered in practice due to the initial overburden of the next printed layer(s), were captured. The slope of the stress-strain response started to drop at around 0.25% and the relatively linear behavior continued on until a strain of 2-5% depending on the material and the time after mixing, which is termed the initial plastic response (still taken as linear) in this work. Beyond that strain, until the stoppage of the test at around 10% strain, the behavior is non-linear. Using the bi-linear response, the elastic and apparent/initial plastic yield stress and moduli of the material were extracted at different times, which were subsequently used in the failure models (considering both material-based and stability-based failures) to determine the theoretical failure height. At any given time, the envelope of the lowest failure heights given by the different failure modes formed the failure curve for that particular material. Experiments using wall and hollow cylinder prints were carried out to determine the failure heights, in order to verify the failure curves from models.

For geometries with lower I/A ratios (e.g., wall section), instability due to buckling/crippling dominated the failure. As the I/A ratio increased (e.g., hollow cylinders), material failure occurred due to the stress exceeding plastic yield stress in the lower filaments, even before the critical height for buckling/crippling failure was reached. The failure curves considered both these approaches, ensuring the robustness of the model in predicting failure heights. The experiments also showed that the wall prints failed predominantly in the buckling or crippling modes, and the corresponding failure curves satisfactorily predicted the failure heights. If the initial elastic response were to be completely ignored and the predictions were made based

solely on a single slope of the stress-strain curve until the plastic yield point (in other words, if the GCT result only used one linear response instead of a bi-linear response), the failure heights would have been significantly underpredicted for buckling collapse. For the cylinder prints, plastic collapse was the dominant failure mechanism at all times for some mixtures, while a transition to buckling/crippling modes were observed for some when the mixtures gained more stiffness. Again, the use of a bi-linear criterion ensures that the predictions are reasonable in such cases. The influence of mixture proportions on buildability at different times can also be understood using the methodology described here, leading to appropriate material design approaches for concrete 3D printing. The methodology laid out in this work can also form the basis for a refined test method to evaluate the buildability of different material designs in layer-wise 3D printing, by combining GCT and actual printing of predefined structural shapes.

6. Acknowledgements

The authors sincerely acknowledge support from U.S. National Science Foundation (CMMI: 1727445; OISE: 2020095) towards this this project. The contents of this paper reflect the views of the authors who are responsible for the facts and accuracy of the data presented herein, and do not necessarily reflect the views and policies of NSF, nor do the contents constitute a standard, specification, or a regulation. The authors acknowledge the support from Salt River Materials Group, Omya, BASF, and Arcosa Lightweight for donating the materials. The authors thank Mr. Harshitsinh Chauhan for his help in printing experiments. We acknowledge the use of 3D printing and material characterization facilities within Laboratory for the Science of Sustainable Infrastructural Materials (LS-SIM) at Arizona State University.

7. References

- [1] N. Labonnote, A. Rønnquist, B. Manum, P. Rüther, Additive construction: State-of-the-art, challenges and opportunities, Autom. Constr. 72 (2016) 347–366. https://doi.org/10.1016/j.autcon.2016.08.026.
- [2] F. Bos, R. Wolfs, Z. Ahmed, T. Salet, Additive manufacturing of concrete in construction: potentials and challenges of 3D concrete printing, Virtual Phys. Prototyp. 11 (2016) 209–225. https://doi.org/10.1080/17452759.2016.1209867.
- [3] G. De Schutter, K. Lesage, V. Mechtcherine, V.N. Nerella, G. Habert, I. Agusti-Juan, Vision of 3D printing with concrete Technical, economic and environmental potentials, Cem. Concr. Res. 112 (2018) 25–36. https://doi.org/10.1016/j.cemconres.2018.06.001.
- [4] M.K. Mohan, A.V. Rahul, G. De Schutter, K. Van Tittelboom, Extrusion-based concrete 3D printing from a material perspective: A state-of-the-art review, Cem. Concr. Compos. 115 (2021) 103855. https://doi.org/10.1016/j.cemconcomp.2020.103855.
- [5] V.N. Nerella, M. Näther, A. Iqbal, M. Butler, V. Mechtcherine, Inline quantification of extrudability of cementitious materials for digital construction, Cem. Concr. Compos. 95 (2019) 260–270. https://doi.org/10.1016/j.cemconcomp.2018.09.015.

- [6] V.N. Nerella, M. Krause, V. Mechtcherine, Practice-Oriented Buildability Criteria for Developing 3D-Printable Concretes in the Context of Digital Construction, (n.d.). https://doi.org/10.20944/preprints201808.0441.v1.
- [7] T.T. Le, S.A. Austin, S. Lim, R.A. Buswell, A.G.F. Gibb, T. Thorpe, Mix design and fresh properties for high-performance printing concrete, Mater. Struct. 45 (2012) 1221–1232. https://doi.org/10.1617/s11527-012-9828-z.
- [8] A. Perrot, C. Lanos, Y. Melinge, P. Estellé, Mortar physical properties evolution in extrusion flow, Rheol. Acta. 46 (2007) 1065–1073. https://doi.org/10.1007/s00397-007-0195-6.
- [9] V.N. Nerella, M.A.B. Beigh, S. Fataei, V. Mechtcherine, Strain-based approach for measuring structural build-up of cement pastes in the context of digital construction, Cem. Concr. Res. 115 (2019) 530–544. https://doi.org/10.1016/j.cemconres.2018.08.003.
- [10] C. Menna, J. Mata-Falcón, F.P. Bos, G. Vantyghem, L. Ferrara, D. Asprone, T. Salet, W. Kaufmann, Opportunities and challenges for structural engineering of digitally fabricated concrete, Cem. Concr. Res. 133 (2020) 106079. https://doi.org/10.1016/j.cemconres.2020.106079.
- [11] Z. Li, L. Wang, G. Ma, Method for the Enhancement of Buildability and Bending Resistance of 3D Printable Tailing Mortar, Int. J. Concr. Struct. Mater. 12 (2018) 37. https://doi.org/10.1186/s40069-018-0269-0.
- [12] N. Khalil, G. Aouad, K. El Cheikh, S. Rémond, Use of calcium sulfoaluminate cements for setting control of 3D-printing mortars, Constr. Build. Mater. 157 (2017) 382–391. https://doi.org/10.1016/j.conbuildmat.2017.09.109.
- [13] B. Panda, S. Ruan, C. Unluer, M.J. Tan, Improving the 3D printability of high volume fly ash mixtures via the use of nano attapulgite clay, Compos. Part B Eng. 165 (2019) 75–83. https://doi.org/10.1016/j.compositesb.2018.11.109.
- [14] B. Panda, J.H. Lim, M.J. Tan, Mechanical properties and deformation behaviour of early age concrete in the context of digital construction, Compos. Part B Eng. 165 (2019) 563–571. https://doi.org/10.1016/j.compositesb.2019.02.040.
- [15] R.J.M. Wolfs, F.P. Bos, T.A.M. Salet, Triaxial compression testing on early age concrete for numerical analysis of 3D concrete printing, Cem. Concr. Compos. 104 (2019) 103344. https://doi.org/10.1016/j.cemconcomp.2019.103344.
- [16] A. Perrot, D. Rangeard, A. Pierre, Structural built-up of cement-based materials used for 3D-printing extrusion techniques, Mater. Struct. 49 (2016) 1213–1220. https://doi.org/10.1617/s11527-015-0571-0.
- [17] N. Roussel, Rheological requirements for printable concretes, Cem. Concr. Res. 112 (2018) 76–85. https://doi.org/10.1016/j.cemconres.2018.04.005.
- [18] T. Wangler, E. Lloret, L. Reiter, N. Hack, F. Gramazio, M. Kohler, M. Bernhard, B. Dillenburger, J. Buchli, N. Roussel, R. Flatt, Digital Concrete: Opportunities and Challenges, RILEM Tech. Lett. 1 (2016) 67–75. https://doi.org/10.21809/rilemtechlett.2016.16.
- [19]T. Di Carlo, Experimental and numerical techniques to characterize structural properties of fresh concrete relevant to contour crafting, Ph.D., University of Southern California, n.d. https://www.proquest.com/docview/1288891920/abstract/DE883E5AFBA4DDAPQ/1 (accessed May 29, 2021).
- [20] T. Di Carlo, B. Khoshnevis, Y. Chen, Manufacturing Additively, With Fresh Concrete, in: American Society of Mechanical Engineers Digital Collection, 2014. https://doi.org/10.1115/IMECE2013-63996.
- [21] L. Casagrande, L. Esposito, C. Menna, D. Asprone, F. Auricchio, Effect of testing procedures on buildability properties of 3D-printable concrete, Constr. Build. Mater. 245 (2020) 118286. https://doi.org/10.1016/j.conbuildmat.2020.118286.

- [22] J. Kruger, S. Zeranka, G. van Zijl, 3D concrete printing: A lower bound analytical model for buildability performance quantification, Autom. Constr. 106 (2019) 102904. https://doi.org/10.1016/j.autcon.2019.102904.
- [23] R. Jayathilakage, J. Sanjayan, P. Rajeev, Direct shear test for the assessment of rheological parameters of concrete for 3D printing applications, Mater. Struct. 52 (2019) 12. https://doi.org/10.1617/s11527-019-1322-4.
- [24] R. Jayathilakage, P. Rajeev, J.G. Sanjayan, Yield stress criteria to assess the buildability of 3D concrete printing, Constr. Build. Mater. 240 (2020) 117989. https://doi.org/10.1016/j.conbuildmat.2019.117989.
- [25] R.J.M. Wolfs, F.P. Bos, T.A.M. Salet, Early age mechanical behaviour of 3D printed concrete: Numerical modelling and experimental testing, Cem. Concr. Res. 106 (2018) 103–116. https://doi.org/10.1016/j.cemconres.2018.02.001.
- [26] M. Dennison, M. Jaspers, P.H. J. Kouwer, C. Storm, A. E. Rowan, F. C. MacKintosh, Critical behaviour in the nonlinear elastic response of hydrogels, Soft Matter. 12 (2016) 6995–7004. https://doi.org/10.1039/C6SM01033D.
- [27] Y. Tanigawa, H. Mori, Analytical Study on Deformation of Fresh Concrete, J. Eng. Mech. 115 (1989) 493–508. https://doi.org/10.1061/(ASCE)0733-9399(1989)115:3(493).
- [28] H. Qiu, Y. Li, T. Guo, S. Tang, Z. Xie, X. Guo, The Effect of Void Arrangement on the Pattern Transformation of Porous Soft Solids under Biaxial Loading, Materials. 14 (2021) 1205. https://doi.org/10.3390/ma14051205.
- [29] J. Zhang, Y. Ju, C. Sun, P. Wang, The Research on Compressive Properties of Polytetrafluoroethylene at High Strain Rate, Def. Technol. 9 (2013) 181–185. https://doi.org/10.1016/j.dt.2013.09.020.
- [30] E.P. Saliklis, T.J. Urbanik, B. Tokyay, Bilinear Modelling of Cellulosic Orthotropic Nonlinear Materials, J. PULP Pap. Sci. 29 (2003) 5.
- [31] M.T.J.J.M. Punter, B.E. Vos, B.M. Mulder, G.H. Koenderink, Poroelasticity of (bio)polymer networks during compression: theory and experiment, Soft Matter. 16 (2020) 1298–1305. https://doi.org/10.1039/C9SM01973A.
- [32] Greenhill, A. G. (1881). "Determination of the greatest height consistent with stability that a vertical pole or mast can be made, and the greatest height to which a tree of given proportions can grow." Proc. Cambridge Philos. Soc., 4, 65–73
- [33] S.P. Timoshenko, J.M. Gere, Theory of Elastic Stability, Courier Corporation, 2009.
- [34] S.A.O. Nair, H. Alghamdi, A. Arora, I. Mehdipour, G. Sant, N. Neithalath, Linking fresh paste microstructure, rheology and extrusion characteristics of cementitious binders for 3D printing, J. Am. Ceram. Soc. 102 (2019) 3951–3964. https://doi.org/10.1111/jace.16305.
- [35] S.A.O. Nair, A. Tripathi, N. Neithalath, Examining layer height effects on the flexural and fracture response of plain and fiber-reinforced 3D-printed beams, (2020).
- [36] B. Panda, M.J. Tan, Rheological behavior of high volume fly ash mixtures containing micro silica for digital construction application, Mater. Lett. 237 (2019) 348–351. https://doi.org/10.1016/j.matlet.2018.11.131.
- [37] A. Perrot, A. Pierre, S. Vitaloni, V. Picandet, Prediction of lateral form pressure exerted by concrete at low casting rates, Mater. Struct. 48 (2015) 2315–2322. https://doi.org/10.1617/s11527-014-0313-8.
- [38] L. Josserand, O. Coussy, F. de Larrard, Bleeding of concrete as an ageing consolidation process, Cem. Concr. Res. 36 (2006) 1603–1608. https://doi.org/10.1016/j.cemconres.2004.10.006.
- [39] N. Roussel, Steady and transient flow behaviour of fresh cement pastes, Cem. Concr. Res. 35 (2005) 1656–1664. https://doi.org/10.1016/j.cemconres.2004.08.001.
- [40] K.V. Subramaniam, X. Wang, An investigation of microstructure evolution in cement paste through setting using ultrasonic and rheological measurements, Cem. Concr. Res. 40 (2010) 33–44. https://doi.org/10.1016/j.cemconres.2009.09.018.

- [41] F. Mahaut, S. Mokéddem, X. Chateau, N. Roussel, G. Ovarlez, Effect of coarse particle volume fraction on the yield stress and thixotropy of cementitious materials, Cem. Concr. Res. 38 (2008) 1276–1285. https://doi.org/10.1016/j.cemconres.2008.06.001.
- [42] L. Reiter, R. Kaessmann, A. Shahab, T. Wangler, R. Flatt, Strategies to wake up sleeping concrete, 2015.
- [43] L. Reiter, T. Wangler, N. Roussel, R.J. Flatt, The role of early age structural build-up in digital fabrication with concrete, Cem. Concr. Res. 112 (2018) 86–95. https://doi.org/10.1016/j.cemconres.2018.05.011.
- [44] A.S.J. Suiker, Mechanical performance of wall structures in 3D printing processes: Theory, design tools and experiments, Int. J. Mech. Sci. 137 (2018) 145–170. https://doi.org/10.1016/j.ijmecsci.2018.01.010.
- [45] R.J.M. Wolfs, A.S.J. Suiker, Structural failure during extrusion-based 3D printing processes, Int. J. Adv. Manuf. Technol. 104 (2019) 565–584. https://doi.org/10.1007/s00170-019-03844-6.